ETH
Eidgenössische Technische Hochschule Zürich
Swiss Federal Institute of Technology Zurich

Department of Physics
Laboratory for Solid State Physics
Quantum Device Lab

Master Thesis

Realization of Temperature and Vibration Measurement Systems for Hybrid Cavity QED Experiments

by Silvio Marx

born in Leipzig, Germany
on October 4, 1985

Supervisor	Dr. Stefan Filipp
Group Leader	Prof. Dr. Andreas Wallraff

Zurich, December 2010

Contents

Abstract

Since the invention of microcomputers and the discovery of quantum mechanics tremendous progress has been made independently in the fields of computing and quantum physics. At the intersection of both fields the field of quantum computing evolved in the last decades. Quantum algorithms are found to outperform their classical counterparts, but the construction of a quantum computer remains still extremely challenging. A viable approach for quantum computation could be the combination of the advantages of different quantum systems. For example, long coherence times of Rydberg atoms can be brought together with fast operation times of superconducting quantum bits on a microchip.

The main objective of this thesis is to understand and characterize a pulse tube cooler system for the manipulation of Rydberg atoms. The temperature at different positions in the experimental setup is measured for different configurations to assess quantitatively the heat loads on the setup. Furthermore, a vibration analysis has been performed to quantify the influence of the pulse tube cooler vibrations on the experiment.

To determine heat loads and system temperatures a temperature controller with silicon diode temperature sensors and resistive heaters is employed. A computer program has been written to log temperature and to control heater power. The sensors have been calibrated individually during the slow warm-up of the system. The cool down duration and the different temperatures of the pulse tube stages, the heat shields and attached electrodes as well as their temperatures for different setup configurations are determined. Based on these data the setup has been optimized and the temperature of the electrodes could be reduced to 4.3K.

The vibration measurement system records the preamplified signal of a geophone vibration sensor. The sensor has been calibrated and used to determine the vertical rms-displacement of the pulse tube cooler and building vibrations of rooms HPF B22 and HPT C4.1 at ETH Hönggerberg. In addition, the time dependence of the rms-acceleration amplitude over at least one day has been measured. A difference between the two rooms could be observed and the pulse tube cooler vibrations could be identified as the dominant source of vibrations.
The investigations in this thesis form the basis of future cryogenic experiments to interface Rydberg atoms with superconducting qubits.

1 Introduction To Hybrid QED Experiments

1.1 Motivation

In the last century among other important things two big improvements have been accomplished.
The first is the development of quantum mechanics which had a tremendous influence on physics and the understanding of the world around us. It describes nature from a probabilistic view point and partially predicts counterintuitive results which is why even leading experts like Albert Einstein rejected this theory. So far there is no consistent and accepted other theory which predicts comparably accurate results. Also no experiment was found to strictly violate quantum mechanics. It enables the understanding of nature also on small atomic scales. New devices like lasers could be built or high precision time measurement devices like atomic clocks. Also for the understanding of nuclear fusion in stars it is necessary to know the behavior of atoms and herewith quantum mechanics broadens the understanding of our surrounding, even beyond the earth.
The second is the invention of the transistor and therewith the revolution of the microcomputer. This technical advancement changed our daily life enormously. The fast computation capability enabled by these integrated circuits has so many applications that it can be used almost everywhere. When assuming a continued increase in performance for future computers comparable with what has been achieved in the last decades the need for a different computing architecture might be questionable. But as microchips become smaller and smaller the influence of quantum effects like tunneling could disturb future advancement.

Quantum effects that pose a problem in current architectures, could also be the key ingredient for a new architecture. Using their special features like superposition and entanglement of quantum states can provide benefits for computing.
In fact, it could be shown that in some cases quantum algorithms are more efficient than their classical counterparts. According to [1] there are three kinds of algorithms found so far:

- First, algorithms based on a quantum version of Fourier transform, like the Shor algorithm for factoring numbers.
- Second type are quantum search algorithms like Grover's algorithm.
- Third, quantum simulations where a quantum computer is used to simulate a quantum system.

But it is not excluded that in the future new algorithms are found. Algorithms have also been implemented already in real quantum computers [2] [3]. The field of quantum computing is

still young and evolves fast but upto now only rudimentary computers could be built. The task to build sufficiently large quantum computers, where sufficient depends on the task, is still an extreme challenging one. New computing architectures have to be invented and the very best properties of different systems should be combined.
The experiment which is in the focus of this thesis aims to combine properties of completely different systems: Rydberg atoms and superconducting resonators and qubits. Despite of these systems being so different they are linked by the property share the property that they can be excited with microwave radiation.
In the course of this introductory part first the physical model will be explained which is needed to understand the very basic properties of the quantum system used for quantum computing. Secondly fundamental properties of Rydberg atoms and the solid state implementation of this physical model will be explained separately. Finally it will be pointed out how these systems can be brought together to form a hybrid setup and advantages of such an approach is discussed.

1.2 Fundamental Physical Model

A promising candidate for quantum computation and quantum information are cavity quantum electrodynamics (cavity qed) systems. There, atoms are placed in a cavity and interact with the quantized electromagnetic fields. When the system is sufficiently decoupled from the surrounding then the quantum nature of the system can be explored. Once this system is understood and can be controlled it could be used for quantum computation and quantum information [4].

To understand the physics of such a system it is best to explore the properties of a minimal version. Hence we deal with a single atom in the cavity only. Even simpler, the atom is reduced to a two level system equivalent to a spin 1/2 and it is coupled to a quantum harmonic oscillator representing the electromagnetic field in the cavity [5]. Such a system is shown in Figure 1.1.

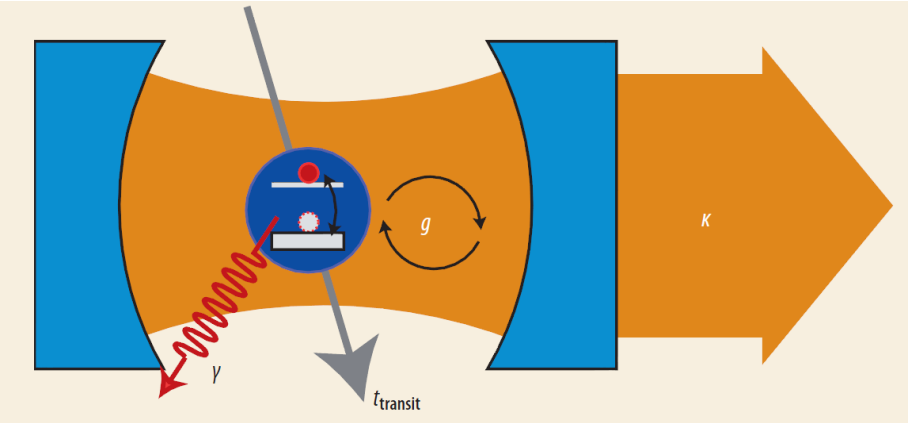

Figure 1.1: Cavity QED model. The figure is taken from [6].

The cavity is formed by two highly reflecting mirrors, drawn in blue. In its interior the quantized electromagnetic field mode is defined by the cavity, drawn in orange. The photons

that represent this mode are reflected several times at the mirrors before leaving the cavity. They leak out of the cavity at a rate κ. Inside the cavity a single two level system is placed. Furthermore it has a ground state ($|g\rangle$ or $|\downarrow\rangle$) and an excited state ($|e\rangle$ or $|\uparrow\rangle$). The excitation decays spontaneously at a rate γ. On resonance, when the photons have the right energy to excite the two level system, the dipole interaction between photons and the two level system takes place at rate g. Furthermore, the time $t_{transit}$ describes the time the two level system spends in the cavity.

According to [7], the system can be described by the Jaynes-Cummings Hamiltonian

$$H = H_r + H_a + H_{ra} + H_\kappa + H_\gamma = \hbar\omega_r \left(a^\dagger a + \frac{1}{2}\right) + \frac{\hbar\omega_a}{2}\sigma_z + \hbar g \left(a^\dagger \sigma^- + \sigma^+ a\right) + H_\kappa + H_\gamma, \quad (1.1)$$

where $\hbar\omega_r$ describes the energy of a single photon in the empty resonator. The operator $a^\dagger$ is the creation operator of a photon with angular frequency ω_r and a is the corresponding annihilation operator. They are defined by

$$a^\dagger |n\rangle = \sqrt{n+1}\,|n+1\rangle\,, \quad (1.2)$$

$$a\,|n\rangle = \sqrt{n}\,|n-1\rangle \quad (1.3)$$

with a photon number state $|n\rangle$ containing exactly n photons. The operators also define the photon number operator

$$\hat{n} = a^\dagger a \qquad \text{with} \qquad \hat{n}\,|n\rangle = n\,|n\rangle\,. \quad (1.4)$$

ω_a is the angular transition frequency between the excited state $|e\rangle$ and ground state $|g\rangle$ of the two level system. H_a describes the state dependent energy of the two level system with the atomic inversion operator defined as

$$\sigma_z = |e\rangle\langle e| - |g\rangle\langle g| \qquad \text{with} \qquad \sigma_z\,|e\rangle = +1\,|e\rangle \text{ and } \sigma_z\,|g\rangle = -1\,|g\rangle\,. \quad (1.5)$$

The third term in Equation (1.1) describes the interaction between photons and the two level system with the atomic raising and lowering operators defined by

$$\sigma^+ = |e\rangle\langle g| \qquad \text{and} \qquad \sigma^- = |g\rangle\langle e|\,. \quad (1.6)$$

They describe the transition to the excited state (σ^+) and the transition to the ground state (σ^-) of the atom. The Hamiltonian H_κ describes the coupling of the cavity to the continuum with the rate κ and the Hamiltonian H_γ describes the decay of the excited state to modes other than the cavity mode [7].

Assuming the ideal case of no damping, we set H_κ=H_γ=0. Then, the Jaynes-Cummings Hamiltonian (Equation (1.1)) has the eigenstates

$$|n,+\rangle = \cos\theta_n |n,g\rangle + \sin\theta_n |n,e\rangle\,, \tag{1.7}$$

$$|n,-\rangle = -\sin\theta_n |n,g\rangle + \cos\theta_n |n,e\rangle\,, \tag{1.8}$$

$$|0,g\rangle \tag{1.9}$$

where $\theta_n = \frac{1}{2}\tan^{-1}\left(\frac{2g\sqrt{n+1}}{\Delta}\right)$ and $|n,+\rangle$ and $|n,-\rangle$ are called dressed states. In case of no interaction ($g = 0$) they are undressed and reduce to $|n,g\rangle$ and $|n,e\rangle$. The eigenenergies are given by

$$E_{n,\pm} = (n+1)\hbar\omega_r \pm \frac{\hbar}{2}\sqrt{4g^2(n+1)+\Delta^2}, \tag{1.10}$$

$$E_{0,g} = -\frac{\hbar\Delta}{2}. \tag{1.11}$$

Here, $\Delta = \omega_a - \omega_r$ is the detuning of cavity and two level system. The energy levels are indicated in Figure 1.2.

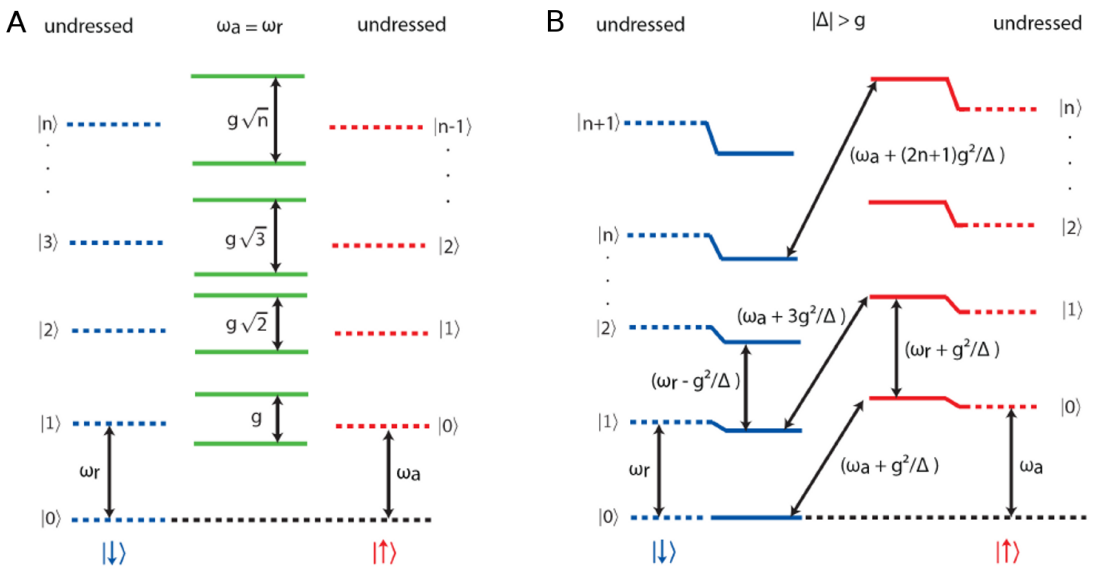

Figure 1.2: Energy levels in the Jaynes-Cummings model. State $|\downarrow\rangle = |g\rangle$ and $|\uparrow\rangle = |e\rangle$. A: resonant case $\Delta = 0$. B: non-resonant case, $|\Delta| > g \neq 0$. Dotted lines are for $g = 0$, solid lines for $g \neq 0$. The figure is taken from [8].

1.3 Circuit QED

The realization is done on a superconducting microchip, see Figure 1.3. A superconducting transmission line resonator plays the role of the cavity. The center conductor of the transmission line in the middle of the light blue structure is surrounded by two ground planes. The electric field is mainly concentrated in the gap between the center conductor and the ground plane. One can think of it as a 2D version of a coaxial cable. A resonator is formed by two

cutouts, where the reflection of photons leads to a standing wave. The resonator is coupled to the continuum via input and output capacitors formed by the cutouts. Furthermore, the microchip is connected to a microwave source that generates the microwave signals. The standing voltage wave that forms in the resonator corresponds to the electromagnetic field in the cavity, shown as orange lines.

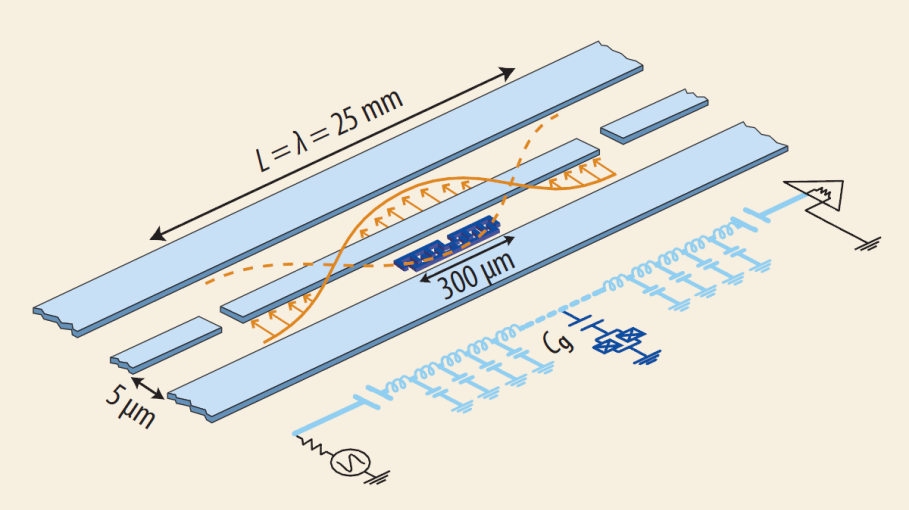

Figure 1.3: Circuit QED model and equivalent lumped element circuit. The figure is taken from [6].

At the voltage antinode of the wave a qubit is placed, shown in dark blue, which leads to a strong electric dipole interaction. It couples capacitively to the center conductor with capacitance C_g. The qubit takes the role of the atom or the two level system.

The qubit is a so called Cooper Pair Box (CPB) that behaves like a giant artificial atom. It is formed by two superconducting areas, the island and the reservoir, that are connected via a Josephson junction with energy E_j and a stray capacitance C_j in parallel (Figure 1.5). In superconductors the charge carriers are bound pairs of electrons, called Cooper pairs, that can travel without energy loss. The Josephson junction allows these Cooper pairs to tunnel coherently between the two areas [9]. Furthermore, the island is voltage biased via the capacitor C_g that electrostatically induces Cooper pairs to tunnel through the Josephson junction. The energy to charge the island with a single electron is given by $E_c = \frac{e^2}{2(C_j+C_g)}$.
The ratio of E_j/E_c is the important parameter to describe the behavior of the system.
When $E_j/E_c \gg 1$ and the qubit with its islands and Josephson junction has a ring like structure, the flux of the qubit is the dominating degree of freedom [10]. The ring structure is also called a SQUID and the flux originates from persistant currents in this ring. The energy states are the two directions the current can flow in the ring [11].
If $E_j/E_c \ll 1$ the system is best described in the charge basis because the energy E_c is the dominating energy scale. The energy of the superconducting island for a charge qubit can be described after [7] as

$$H_{CPB} = 4E_c \sum_N (N - N_g)^2 \left|N\right\rangle \left\langle N\right| - \frac{E_j}{2} \sum_N (\left|N+1\right\rangle \left\langle N\right| + \left|N\right\rangle \left\langle N+1\right|), \tag{1.12}$$

where N is the number of Cooper pairs on the island and $N_g = C_g V_g/2e$ the gate charge in units of Cooper pairs induced via the capacitor C_g and the applied voltage V_g. From the second part of the Hamiltonian we see that E_j is the characteristic energy of the potential barrier in the Josephson junction where the Cooper pairs tunnel through and therefore defines the coupling between the two superconducting areas. The energy of the CPB as a function of gate charge is shown in Figure 1.4.

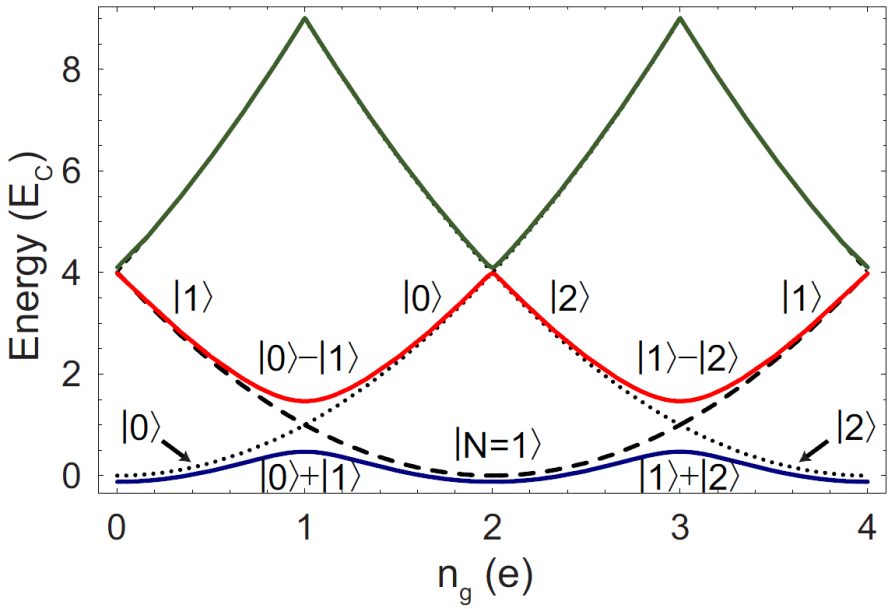

Figure 1.4: Cooper Pair Box energy levels. The number of induced electrons on the island is $n_g = 2N_g$. Dashed and dotted lines show the energy levels for E_j=0 and N=0, 1 or 2 Cooper pairs on the island. Solid lines show the situation for E_j=E_c. They represent the ground state (blue) and the first two excited states (red, green). There is an avoided crossing for odd n_g and the eigenstates are equal superpositions of the pure states $|N\rangle$ and $|N+1\rangle$. The figure is taken from [9].

The lowest two energy levels are typically used as the two level system, the qubit, with states $|g\rangle$ (blue solid line) and $|e\rangle$ (red solid line). Manipulating a system with multiple qubits like these with microwave pulses corresponds to calculations with a quantum system.
To get an impression of a real microchip see Figure 1.5.

1.4 Rydberg Atoms

Now we turn to the properties of Rydberg atoms, the second system we want to use in the planned experiments.
Rydberg atoms are atoms excited to high energy states [13]. More precisely, they have a principle quantum number $n \gtrapprox 10$. Their properties are very different from atoms in lower n states, see Table 1.1.

The inverse quadratic dependence of energy levels in atoms was already found by Balmer in 1885 and could be explained by Bohr's theory of the atom [13] even before the advent of modern quantum mechanics.

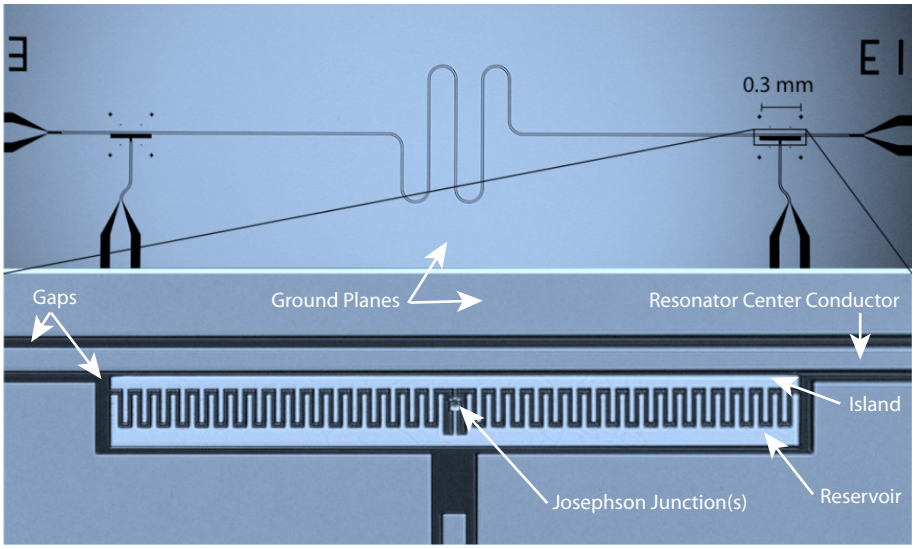

Figure 1.5: Microchip with two transmon qubits. These qubits are "split" Cooper pair boxes because they have two Josephson junctions. With this feature the energy E_j can be tuned through a magnetic flux [9]. The photograph is taken from [12].

Property	n dependence	Na(10d)
Binding energy	n^{-2}	0.14eV
Energy between adjacent n states	n^{-3}	0.023eV
Orbital radius	n^2	$147a_0$
Dipole moment $\langle nd\vert\, er\,\vert nf\rangle$	n^2	$143ea_0$
Radiative lifetime	n^3	$1.0\mu s$

Table 1.1: Selected Rydberg atom properties and example values for the state n=10 and l=3 in Na. Table from [13].

The n^2 behavior of the orbital radius of the electron could also be explained by the Bohr theory from the classical circular motion of the electron around the nucleus and the quantization of angular momentum [13]. This behavior indicates the fast increasing size of the atom for high n states. The comparison with the Bohr radius $a_0 = \frac{\hbar}{m_e c \alpha} \approx 0.053nm$ (m_e: electron rest mass, α: fine structure constant) shows that the atomic size could reach the μm scale for $n = 100$. This is extremely large for a single atom.

Since the binding energy scales with n^{-2} the high energy states with large n are close to the ionization threshold compared to the ground state. Therefore relatively weak electric fields can have a big influence on the state of the electron and potentially ionize the atom.

Furthermore it is interesting that the lifetime of the Rydberg atoms increases with the cube of the principle quantum number n. The lifetime of Na(n=10,l=3) is $1.0\mu s$ even for a comparably low Rydberg state (n=10). For more realistic levels ($n = 10...100$) the lifetimes are the order of $\mu s - ms$ which is large compared to current transmon qubits [14].

Interaction with an electric field

Rydberg atoms exhibit also the Stark effect when they are exposed to an electric field. This means the spectral lines are shifted by the field in general.

The shift of the lines for hydrogen and sodium are shown in Figure 1.6. For states with fixed principal quantum number n and magnetic quantum number $|m|$ there are $n - |m|$ Stark levels in hydrogen [13]. Levels can be shifted up or down in energy. In hydrogen the levels of different n cross for sufficiently large electric fields. In sodium the s and p states have large quantum defect due to the interaction with the core and have therefore different energies than the higher l states which behave more like hydrogenic energy levels. A further difference between the two atoms is, that in sodium lines with different n show an avoided crossing. This originates from the overlap of wavefunctions of adjacent n manifolds in sodium and is not present in hydrogen in non-relativistic treatment [13].

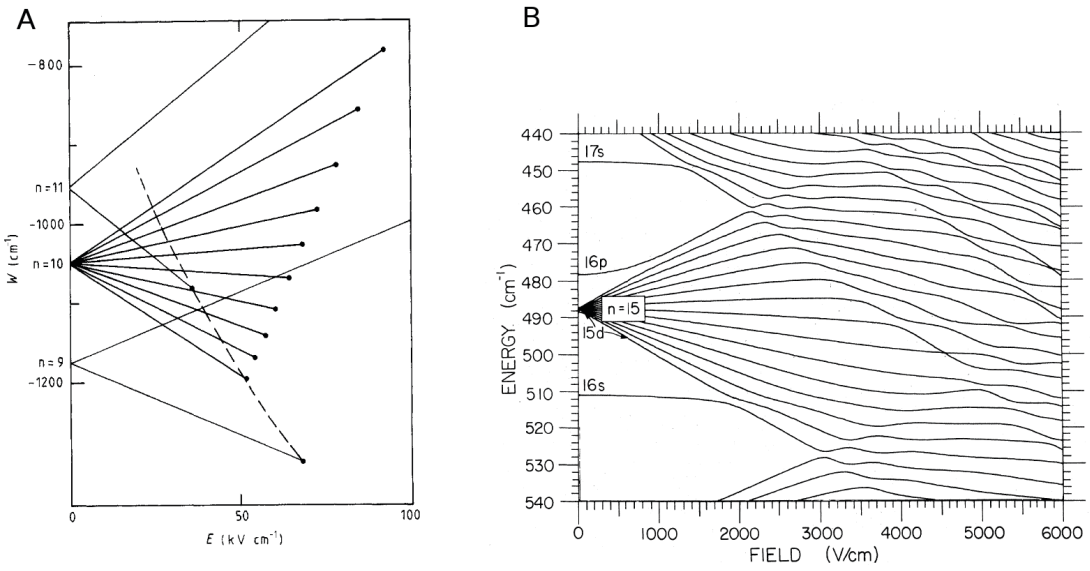

Figure 1.6: Stark shifted energy levels for H and Na. A: Calculated Stark shift for hydrogen in an electric field for quantum number $m = 0$. Vertical axis is energy, horizontal is electric field strength. Extremes of $n = 9$ and $n = 11$ are indicated. B: Behavior of Na energy levels in electric field for $m = 0$. Figure A is from [15] and B from [16].

That the lines in hydrogen shift nearly linear with the applied electric field shows that they have a permanent electric dipole moment. By lifting the degeneracy of the levels with an applied electric field one has a method of selecting states of Rydberg atoms. This can be used to guide them in the experiment since its response to electric fields is known.

1.5 Hybrid Cavity QED Systems

The term "hybrid system" means the use of different kinds of systems in one experimental setup. These single species systems have been studied intensively and have their specific weaknesses and advantages.

Systems include single and many atom properties exploited in ion traps and addressed via lasers [3]. Also the nuclear spins in neutral atoms/molecules [17] and Rydberg atoms [18] in optical cavities and have been studied before.

Quantum gates were implemented in quantum dot based two level systems [19] and in solid

state based setups like Cooper pair box qubits in transmission line cavities coupling of two qubits could be achieved [20].
To go a step further in the investigations it could provide useful use the advantages of the systems studied before. Figure 1.7 illustrates properties of various quantum systems. Clearly observable are the extremely different properties. They can be several orders of magnitudes different.

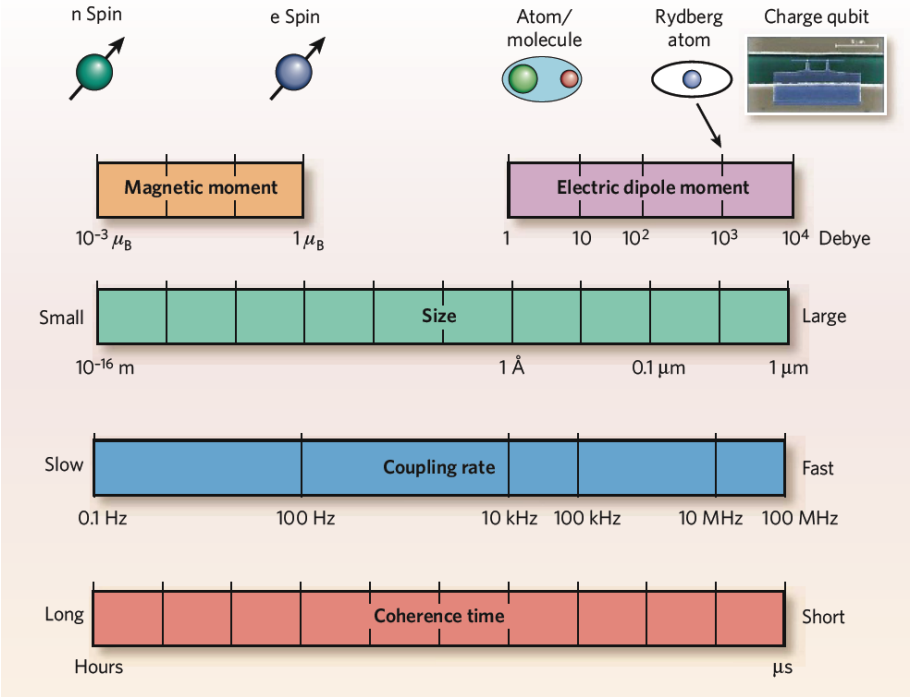

Figure 1.7: Properties of different quantum systems for QED experiments. Properties include the electric and magnetic dipole moments (top bar), the required transverse size of a cavity to obtain maximal coupling (second bar), their coupling rates to a 1μm cavity (third bar) and the expected life times of coherent superpositions (bottom bar). The figure is taken from [21].

In the focus of our experiments is the combination of Rydberg atoms with superconducting transmission line cavities and solid state qubits like the Cooper pair box which could interact via microwave photons. Of primary interest is the longer coherence time of Rydberg states over the solid state qubits in combination with the fast control in solid state systems and the scalability of the microchip architecture used so far. The increased life time of Rydberg Stark states could compensate the lower coupling rate.
To compare the life times and coupling rates is essential because for a quantum computer it is important how many operations can be done before the information in the qubit is lost.
A technique for coupling of Rydberg atoms to a superconducting transmission line was already proposed [22]. The large electric dipole moment of the Rydberg atoms induces voltage fluctuations in the transmission line. For instance excitations could be transfered from the Rydberg atom to the transmission line or atoms could be entangled.
The coherent interaction between cavity and Rydberg atoms was also shown before [23]. Entanglement between Rydberg atoms and between Rydberg atoms and cavity photons were established which is a key ingredient in quantum logic gates and qubit state preparation.

In the planned experiment a cloud of Rydberg atoms will by guided with electric fields to fly over the resonator and interact with its electric field. The final goal is to trap only a single Rydberg atom to strongly interaction with the resonator and/or qubit. Then the individual advantages of the systems like longer coherence times of the Rydberg atoms and fast control of the solid state qubit can be exploited.

2 Experimental Setup

2.1 Overview

To reach the goals of the project an experimental setup must be realized. From the experiences of the involved groups of Prof. Wallraff and Prof. Merkt in their area of research a prototype setup will be built. It will first serve as a testing ground to explore the feasibility of the project and to begin with experiments. Figures 2.1 and 2.2 show the vacuum chamber and related parts of the experimental setup. The complex laser setup is not shown but the use of the laser beam is mentioned in the explanation of the working principle later in the text.

The setup consists of a pulse tube cooler in a vacuum chamber. The pulse tube cooler has two stages: stage 1 at approximately 30K temperature and stage 2 at approximately 3K temperature at the bottom. At the second stage the superconducting microchip together with electrodes is located. To shield the setup from (thermal) radiation and magnetic fields, four metallic boxes surround the sensitive parts, see Figure 2.1B. One shield is in good thermal contact with each stage to reduce thermal radiation in the interior. In addition two metallic Cryoperm® shields with high magnetic permeability are reducing magnetic fields.

Gas as a coolant is let in and out of the pulse tube cooler at a frequency of 1.4Hz. This causes vibrations. To reduce the influence of the vibrations on the experiment the pulse tube cooler is mounted on springs on top of the vacuum chamber, Figure 2.1E. Furthermore, the rotating valve that controls the gas flow is remotely connected to the pulse tube. In the moment the sampleholder, the microchip and the electrodes are rigidly connected to the the pulse tube cooler and the walls of the vacuum chamber. For even further reduction of vibrations they could also be flexibly connected to the pulse tube stage.

For an overview of the experimental layout inside the chamber, see Figure 2.2. A source of ammonia molecules which serves as a hydrogen source is connected to the vacuum chamber. A pulsed valve releases the molecules to the vacuum. Then hydrogen atoms are photodissociated from the ammonia molecules when they absorb photons from an Excimer laser beam. A skimmer is inserted along the path of the beam that provides a beam of atoms to the experiment with small divergence. Dye lasers are used to excite the hydrogen atoms in the beam to Rydberg states. At the time the atoms get excited by the lasers they are located between two electrodes. The electric field between the electrodes will shift the transition frequencies between the atomic energy levels because of the linear Stark effect and also lifts the degeneracy of the energy levels. Then one can select transitions to the Stark shifted energy levels with a clearly defined dipole moment which enables more precise control over the motion of the atoms in the present electric fields of the on-chip atom guide. After passing the first two

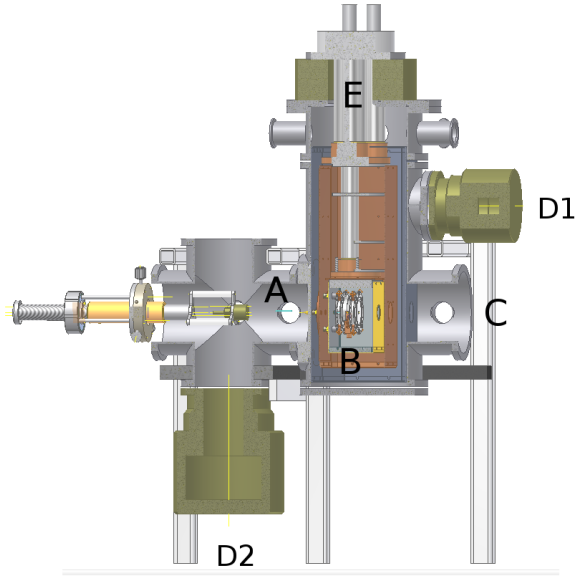

Figure 2.1: Drawing of the vacuum chamber. Atoms fly from left to right. A: Molecules enter the vacuum chamber and hydrogen atoms are prepared. B: Region where the atoms are excited to Rydberg states, the interaction with the microchip takes place and the field ionization occurs. C: position of the ion detector. D1 & D2: Vacuum pump systems. E: Pulse tube refrigerator to cool the micro chip.

electrodes (Figure 2.2D) the beam enters the region of the sample holder with the microchip. There, the atoms can be guided and trapped above the on-chip structures and interact with the microwave resonator. After being manipulated they leave the area of the chip and enter the region between two electrodes shown in Figure 2.2F. Here, a large electric field is applied to ionize the atoms. The ionization clearly depends on the magnitude of the field and the state of the atoms, allowing for state selective detection.

2.2 Parts Of The Setup

In this section the working principle of the individual parts of the setup is explained in more detail. The explanations contain the vacuum pump system for low pressure, the pulse tube refrigerator for cooling, the lasers for creation of Rydberg states, the detection of the Rydberg states with a microchannel plate detector and the cabling scheme in the cryostat. The exterior and interior of the setup as well as the used heat shields are pictured, too.

2.2.1 The Vacuum System

For the Rydberg atoms to be decoupled from their surrounding it is necessary to provide a high vacuum in the vacuum chamber. This is done with two specialized pumps: a piston pump and a turbomolecular pump, indicated in Figure 2.1D1 and D2. The turbomolecular pump is directly connected to the vacuum chamber and the piston pump is placed behind it.

The first pump is a *Pfeiffer Vacuum XtraDry* ^{TM} *150-2* piston vacuum pump. It reduces the pressure from atmospheric pressure, roughly 10^3 mbar, to approximately 10^{-1} mbar. The

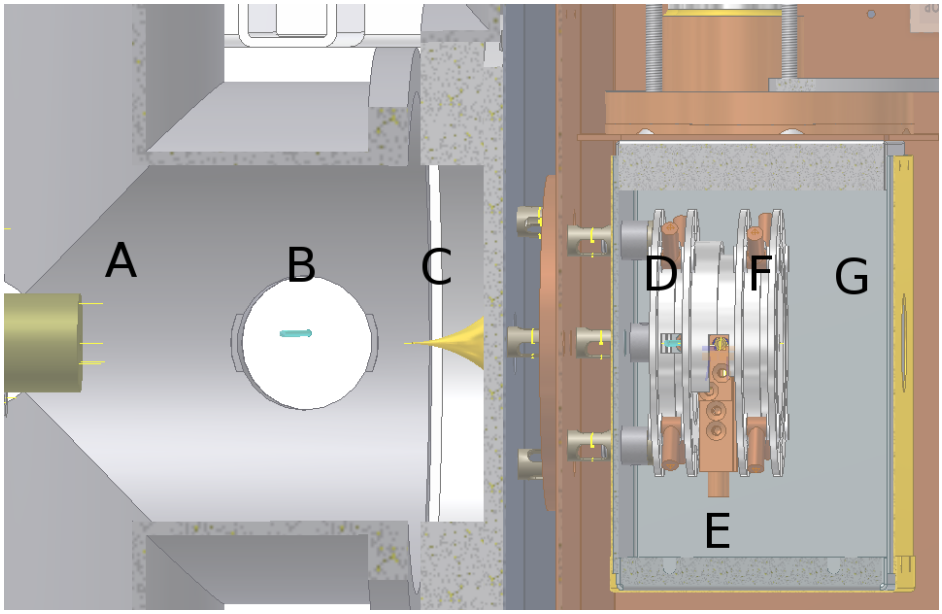

Figure 2.2: Zoomed view of the inner part of Figure 2.1. A: Ammonia molecules are released to the vacuum with a pulsed valve (green cylinder). B: Photolysis with an Excimer laser beam splits hydrogen atoms from ammonia molecules. C: A skimmer provides a narrow hydrogen beam for the experiment. D: First two electrodes for the Stark splitting of energy levels as well as the excitation to Rydberg states by absorbing two photons from dye lasers. E: Sample holder with the micro chip on top (covered). F: Electrodes for field ionization. G: Ions are accelerated towards the microchannel plate detector ("MCP").

pump consists of two compression stages that are connected in series. The gas from the vacuum chamber enters the first stage and will be compressed. Afterwards the gas will be displaced to the second compression stage where its pressure is increased above atmospheric pressure. Finally it will be released to the surrounding. Then the cycle repeats with new gas from the vacuum chamber entering the pump.

The second pump is a *Pfeiffer Vacuum TMH 261 P* turbomolecular pump and requires a fore-vacuum with pressure ≤ 5 mbar. Technically spoken the pump is a turbine with stacked rotors and inclined rotor blades that spins with a frequency of 1000Hz. When molecules from the vacuum chamber come in contact with the spinning rotor blades they will be adsorbed to the surface for a short time [24]. In this time span momentum will be transfered to them in the outwards direction. Therefore they will leave the chamber and the pressure will decrease further to approximately 10^{-7} mbar.

More detailed information about both vacuum pump systems is available at [24, pages 40ff. and 57ff.].

2.2.2 The Cryogenic System

To provide low enough temperatures for the superconducting parts of the setup like the coplanar waveguide resonator or the qubits on the chip, a cooling system must be used. The minimum temperature should be below 5K to achieve the superconducting state of the chip

material to reduce dissipation of the microwave field in the material.
In this setup the *Cryomech PT415RM* pulse tube refrigeration system together with the *Cryomech CP1000* helium compressor is used with a minimum temperature of 2.7K.
The working principle of the pulse tube is comparable to a Stirling type heat pump with a regenerator, explained below. The explanation of the principles follows reference [25].

Stirling Heat Pump

The Stirling heat pump, left sketch in Figure 2.3, relies on the expansion and compression of a working gas in a closed cycle at different positions in the heat pump. The major parts of the setup are: first a moving working piston which creates an oscillating pressure by using a power of $\dot{W}_0$. Second a displacer which displaces the working gas from the cold end at the bottom to the hot end and vice versa. Finally a regenerator which acts as a heat reservoir. It precools and heats the gas when flowing between the hot and the cold parts.

When the cycle begins, the gas is mostly in the working piston at the top of the sketch in Figure 2.3(a). The working piston moves down, compresses and heats the working gas. While the heated gas flows down it comes in contact with the heat exchanger and releases the heat of compression there. This heats the heat exchanger to a temperature T_0 and provides the surrounding with a thermal load of $\dot{Q}_0$. Afterwards the displacer is moved up and the gas flows through the regenerator. Since the regenerator is a tube filled with a material of large surface and a high heat capacity, it takes up heat from the flowing gas easily without large temperature increase. The precooled gas reaches the lower end of the system. Then the working piston is moved up such that the gas is expanded and cooled. The cooled gas then takes up energy from the heat exchanger at the bottom with a rate $\dot{Q}_c$ and cools the heat exchanger to a temperature T_c. Finally the displacer moves down and forces the gas back through the regenerator to the hot end of the system. The regenerator will release energy to the cold gas before it reaches the hot end. This role as an energy reservoir increases the efficiency significantly since this depends on the temperature difference of the hot and the cold part and the regenerator increases this temperature difference. After the gas reaches the warm end, the cycle will begin again. In this cycle it is important that the displacer moves in such a way that the mass flow between the cold and the hot end of the gas is approximately in phase with the pressure. In this way a net power flows towards the hot end. If there was no displacer, the gas temperature would oscillate at the same place which would not produce a temperature gradient.

Pulse Tube Refrigeration

The pulse tube refrigerator works in close analogy to the Stirling heat pump. A sketch of a single stage orifice pulse tube cooler can be seen on the right side of Figure 2.3. It consists of a moving piston in a compressor, located far away from the pulse tube system and uses a power of $\dot{W}_0$ to compress the gas. Furthermore a regenerator is put between the cold and hot ends of the system to increase the efficiency. The displacer from the Stirling heat pump is exchanged with an orifice and a reservoir. This has the advantage that there are no moving parts in the setup except the gas. This reduces vibrations and heating due to friction in

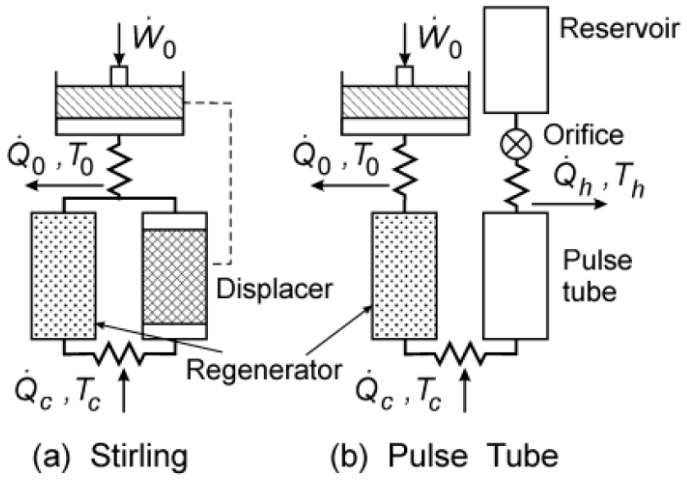

Figure 2.3: Comparison between Stirling heat pump and pulse tube refrigerator. The figure is taken from [25, fig. 2].

the vicinity of the cold heat exchanger where the cooled objects are located and increases the lifetime of the pulse tube. The orifice is a flow impedance and when tuned correctly the gas flow will be approximately in phase with the pressure. Therefore the oscillating gas flow through the orifice will separate the cooling and heating effects in the same way the displacer would do in the Stirling heat pump. It delays the flow of the gas such that it introduces a phase shift between the two pistons. The pulse tube itself is simply a hollow tube filled with the working gas.

The cycle begins with a pressure increase provided by the compressor. Heat of compression is released to a heat exchanger at a rate $\dot{Q}_0$ near the working piston and heats the heat exchanger to a temperature T_0. Then the gas is already precooled when it flows through the regenerator. The pressure increase in the pulse tube will lead to an increase of the gas temperature since ideally the process is adiabatic and no heat is exchanged with the surrounding. Since the pressure in the pulse tube is now higher than the pressure in the reservoir the gas at the upper end of the pulse tube will start to flow through the orifice towards the reservoir. The temperature variation in the reservoir is very small since it has a large volume. On its way it will heat up the heat exchanger to temperature T_h and release energy at a rate $\dot{Q}_h$ to the surrounding when it is in contact with the heat exchanger. The gas in the lower part of the pulse tube is moved up and heated too, but is not in contact with the cold heat exchanger at this part of the cycle. Next the pressure is reduced and the gas will expand nearly adiabatically. Therefore the gas in the reservoir will flow back towards the pulse tube and will cool down in the pulse tube. Since it is not in contact with the heat exchanger when it cools no heat is transfered to it. Gas in the vicinity of the cold heat exchanger in the pulse tube is cooled too and as it flows in the direction of the regenerator it will take up heat from the heat exchanger at a rate $\dot{Q}_c$. Gas in the middle of the pulse tube will never leave the pulse tube and insulates the processes at the cold and hot end. It does this because it prevents the gas at the cold and hot end to reach the other side. In order to do this, the pulse tube must be long enough that gas entering the pulse tube has not enough time to traverse

the whole pulse tube before the flow is reversed. Furthermore for an efficient insulation it is necessary to avoid turbulent flow in the tube. Therefore, flow straightening at the two ends is crucial for the operation. If these requirements are fulfilled, the gas in the middle will form a temperature gradient between the two ends of the pulse tube. This middle part of the pulse tube can be seen as a displacer consisting of gas.

For an overview about the pulse tube system used in the experimental setup see Figure 2.4. The figure shows the two connected pulse tube systems. The first system consists of parts D, E, F, J and A. Parts D, E, G, H, I and B belong to the second pulse tube system. The first part of the regenerator (E) is used by both systems. Therefore the gas that enters the second part of the regenerator (G) is precooled by the first stage pulse tube (J) already. The two reservoirs of the two pulse tube systems are connected to A and B. The compressor that provides the high and low pressure is connected to C. In addition to the precooling of the pulse tube stage 2 a metallic shield is connected to the stage 1 (F) that shields stage 2 (H) from radiation. Additionally cables from the outside of the vacuum chamber (temperature approximately 300K) are thermalized at both stages to prevent the inner part of the setup to warm up. The inner part of the setup which contains several electrodes, the sample holder and the microchip is connected to stage 2 of the refrigeration system, Figure 2.1B/E.

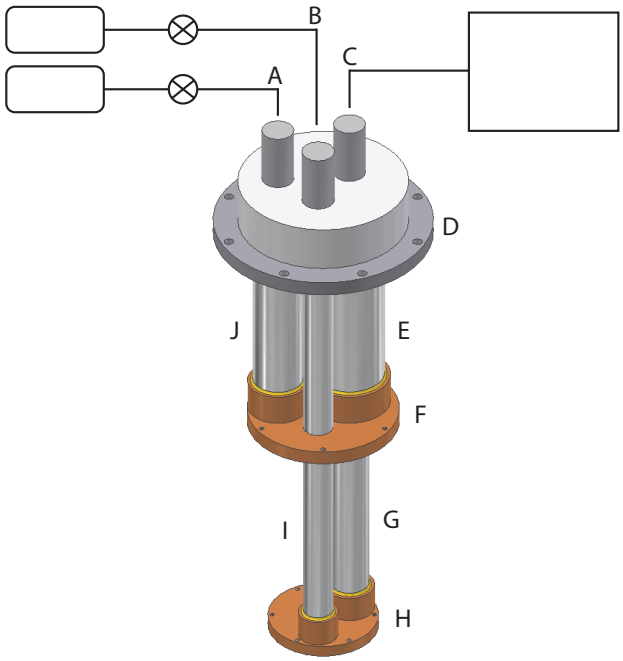

Figure 2.4: Refrigeration system with two pulse tubes. A & B: to reservoirs through an orifice. C: Connection to the compressor. D: Heat exchanger to the surrounding. E & G: Regenerators, E is used by both pulse tubes. F & H: Cooling stages 1 and 2. I & J: Pulse tubes 2 and 1.

2.2.3 Lasers And Rydberg States

For the preparation of atoms in Rydberg states several steps are needed. The first step is to produce free hydrogen atoms. This is done by photolysis of NH_3 (ammonia) into NH_2

and H which means that the hydrogen atom dissociates from the molecule with the help of a laser. The energy needed to overcome the binding energy of the hydrogen in the molecule are provided by photons from a pulsed Excimer laser. In this laser an argon fluoride gas (ArF) is excited by an electric discharge to prepare the population inversion state. The gas is put in a cavity formed by two mirrors and emits laser radiation with 193nm wavelength used for the dissociation process. The Excimer laser, the photolysis laser beam and the gas beam (NH_3, "probe gas") are indicated in Figure 2.5.

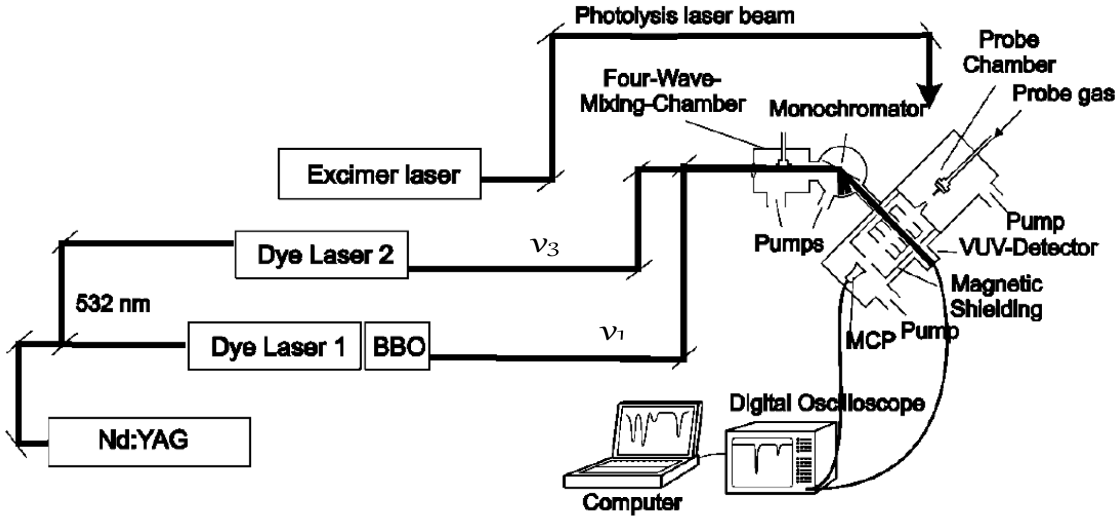

Figure 2.5: Diagram of the experimental setup for the production of the 121nm wavelength radiation by four wave mixing as well as the photolysis region ("probe chamber") and detection region ("MCP"). The photolysis laser beam will interact with the ammonia molecules in the probe chamber. Between these two regions the atoms are excited to Rydberg states(not shown), the interaction with the micro chip will take place(not shown) and the atoms will be ionized. The figure is taken from [26, fig. 1].

In a second step, the hydrogen atom are excited to a state with high principle quantum number n. This is done by absorbing two photons. From the ground state with n=1 the hydrogen atoms are excited with 121nm wavelength radiation (Lyman-α line of the hydrogen spectrum) to the n=2 energy level. The production of this radiation is done in a four-wave mixing process, as shown in Figure 2.5. Four-wave mixing relies on a third order nonlinearity in the susceptibility of a medium. Here, krypton gas provides this nonlinearity. Three incident photons with frequencies ν_1, ν_2 and ν_3 will produce a new photon of different frequency ν_4. There are several frequency possibilities for ν_4, but only one is of interest here:

$$\nu_4 = \nu_1 + \nu_2 - \nu_3. \tag{2.1}$$

Other frequencies from the four wave mixing process are rejected with the help of a monochromator. Since ν_1=ν_2 in our setup, we have

$$\nu_4 = 2\nu_1 - \nu_3. \tag{2.2}$$

Dye laser 1 and Dye laser 2 are pumped by a green Nd:YAG laser to produce the two dif-

ferent frequencies needed. Frequency $2\nu_2$ is resonant with a transition in krypton and ν_3 is tuned such that the resulting frequency ν_4 is resonant with the n=1 to the n=2 transition in hydrogen. The frequencies are: ν_1=212.55nm, ν_3=843nm and ν_4=121.6nm.

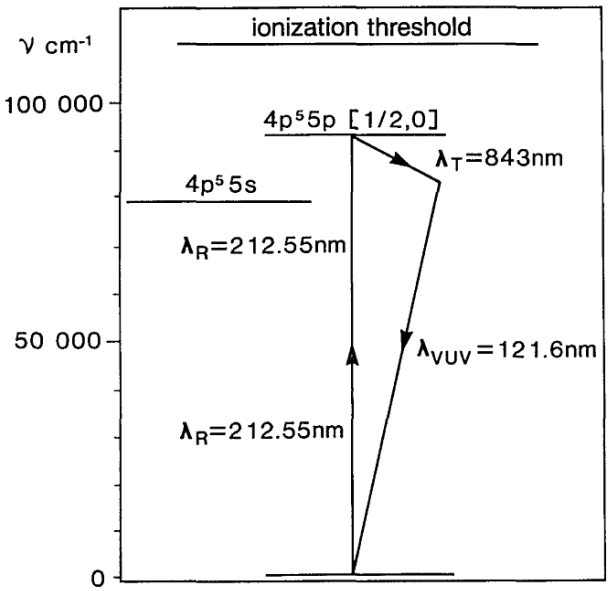

Figure 2.6: Partial energy level scheme of krypton showing the resonance-enhanced four-wave mixing for the production of the λ_{VUV}=121nm radiation. The vertical axis is frequency. λ_R and λ_T indicate resonant and tunable wavelengths and correspond to ν_1 and ν_3. The lowest energy level is the [Ar] $3d^{10}$ $4s^2$ $4p^6$ electronic ground state configuration of krypton. [Ar] denotes the electronic ground state configuration of the noble gas argon. The figure is taken from [27, fig. 1]

To excite the hydrogen atoms from the n=2 to higher states, a second photon is needed. The green Nd:YAG LASER pumps another dye LASER emitting 728nm-736nm wavelength photons. These are frequency doubled in a Beta barium borate (BBO) crystal to 364nm-368nm. Transitions from n=2 to n=20-100 are possible with photons of a wavelength is this interval. The resulting Rydberg atoms can then be used in the experiment.

2.2.4 Detection Of Rydberg States

After the preparation of the Rydberg states and the interaction of the atoms with the microchip it is necessary to obtain information about the interaction and the states of the Rydberg atoms. This is done in two steps.

First, the Rydberg atoms are field ionized in the electric field produced by a potential difference between two metallic electrodes. With the careful choice of the electric field strength the atoms can be ionized depending on their state after the interaction.

Second, the produced ions must be detected. This is done with a microchannel plate detector ("MCP"), sketched in Figure 2.7. The MCP consists of a glass structure with about 10^4-10^7 channels parallel to each other. The diameter of a single channels is typically 10μm-100μm and the length is 40-100 times the diameter. The main working principle of the MCP is the secondary electron emission from the walls of the tubes. Between the two faces of the MCP

a voltage is applied. The ions are accelerated towards the MCP and when hitting the wall of a tube they knock out electrons. These electrons are accelerated by the applied voltage and will hit the wall several times. Then new electrons are released, creating an avalanche effect. In the end the device acts as an electron multiplier. Multiplication factors of 10^4-10^7 are typical. Then the resulting current can be measured or the electrons hit a fluorescent sheet and the emitted light is monitored by a camera. For further detailed information about the microchannel plate detector, see Reference [28].

With this measurement scheme it is possible to obtain information about the states of the Rydberg atoms that also allows to draw conclusions about the interaction with the on-chip structures like the resonator and the qubit.

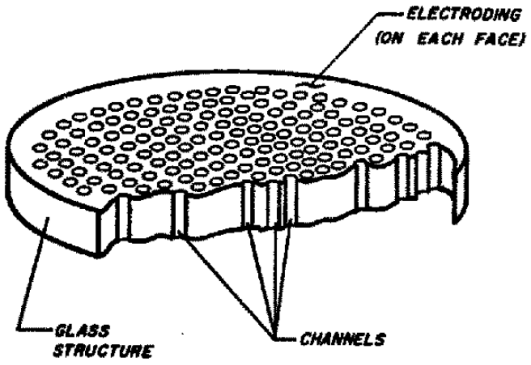

Figure 2.7: Sketch of a microchannel plate detector. The figure is taken from [28, fig. 1]

2.2.5 Devices And Cables

To control and measure temperature, electric fields and microwaves the setup has to be equipped with various devices and cables. The setup configuration is shown in Figure 2.8.

Connected to the two stages of the pulse tube cooler are many thermalizations ("Th.") for the cables entering the chamber from the outside. This is because the cables transport heat from room temperature to the colder parts of the setup. To prevent the microchip from heating up due to the heat transport via the cables, they are glued and wound around copper cylinders which are fixed to the stages. The large contact area allows for proper heat exchange at these posts. In addition there are interconnections between cables from the outside to devices like temperature sensors and heaters as well as low voltage electrodes and the microwave resonator on the chip. They are indicated as "IC". The heater is a resistor that dissipates heat when current flows. It can be used to stabilize the temperature with a feedback loop controlled by the temperature controller.
Photographs of the cryostat and pulse tube cooler can be seen in Figure 2.9, the shields and spacers are shown in Figure: 2.10. Temperature controller cabling schemes and pin descriptions are given in Appendices.

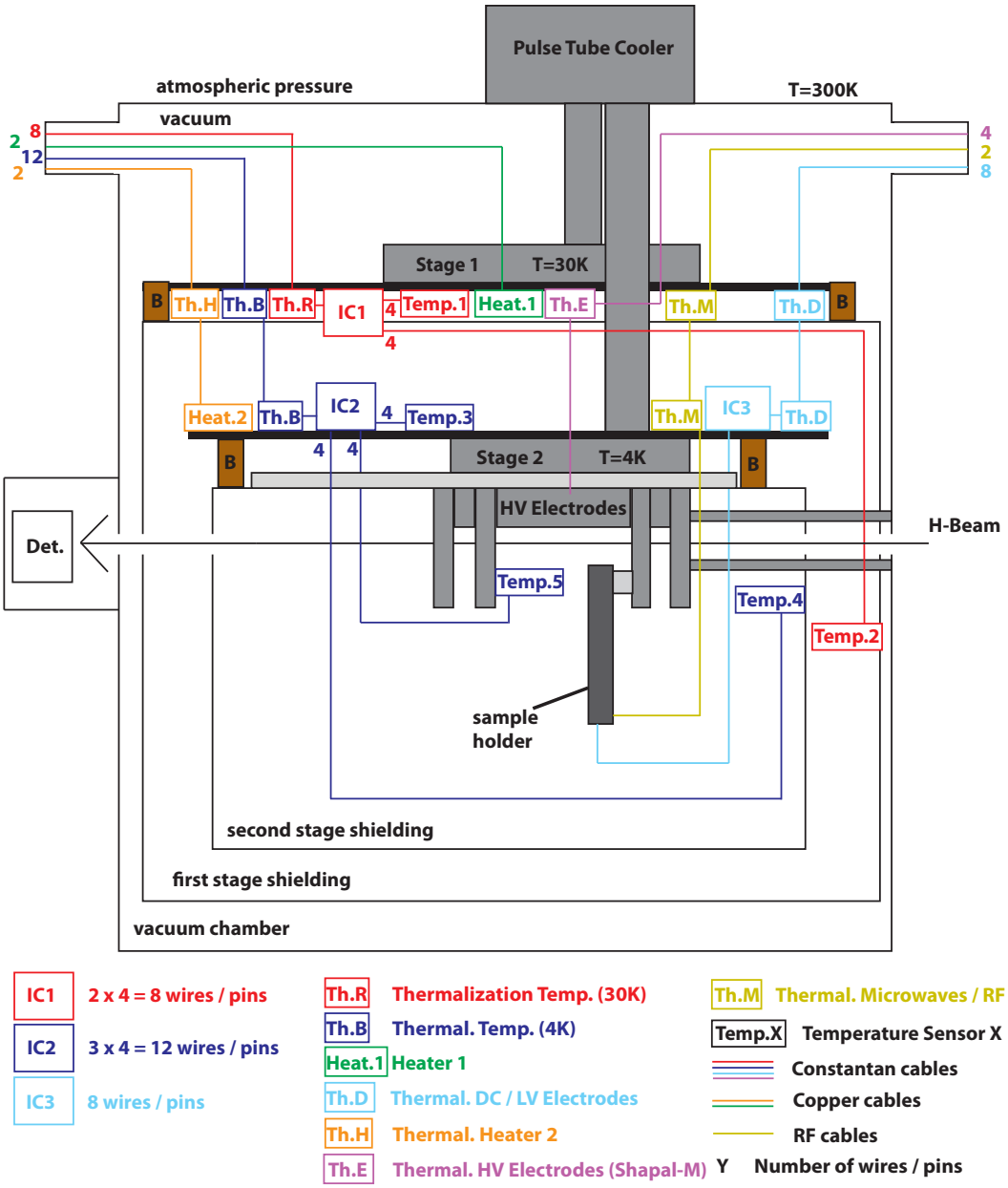

Figure 2.8: Devices and cables in the vacuum chamber. The position of various cables, thermalizations ("Th."), temperature sensors ("Temp.") and heaters ("Heat.") as well as interconnections between cables ("IC") are indicated. From the upper left flange of the figure all temperature related cables are entering the vacuum chamber. From the upper right flange the cables for the high voltage electrodes ("HV") for ionization and Stark state preparation, the low voltage DC electrodes for guiding on the chip ("DC/LV") as well as the microwaves ("RF") are feed in the vacuum chamber.

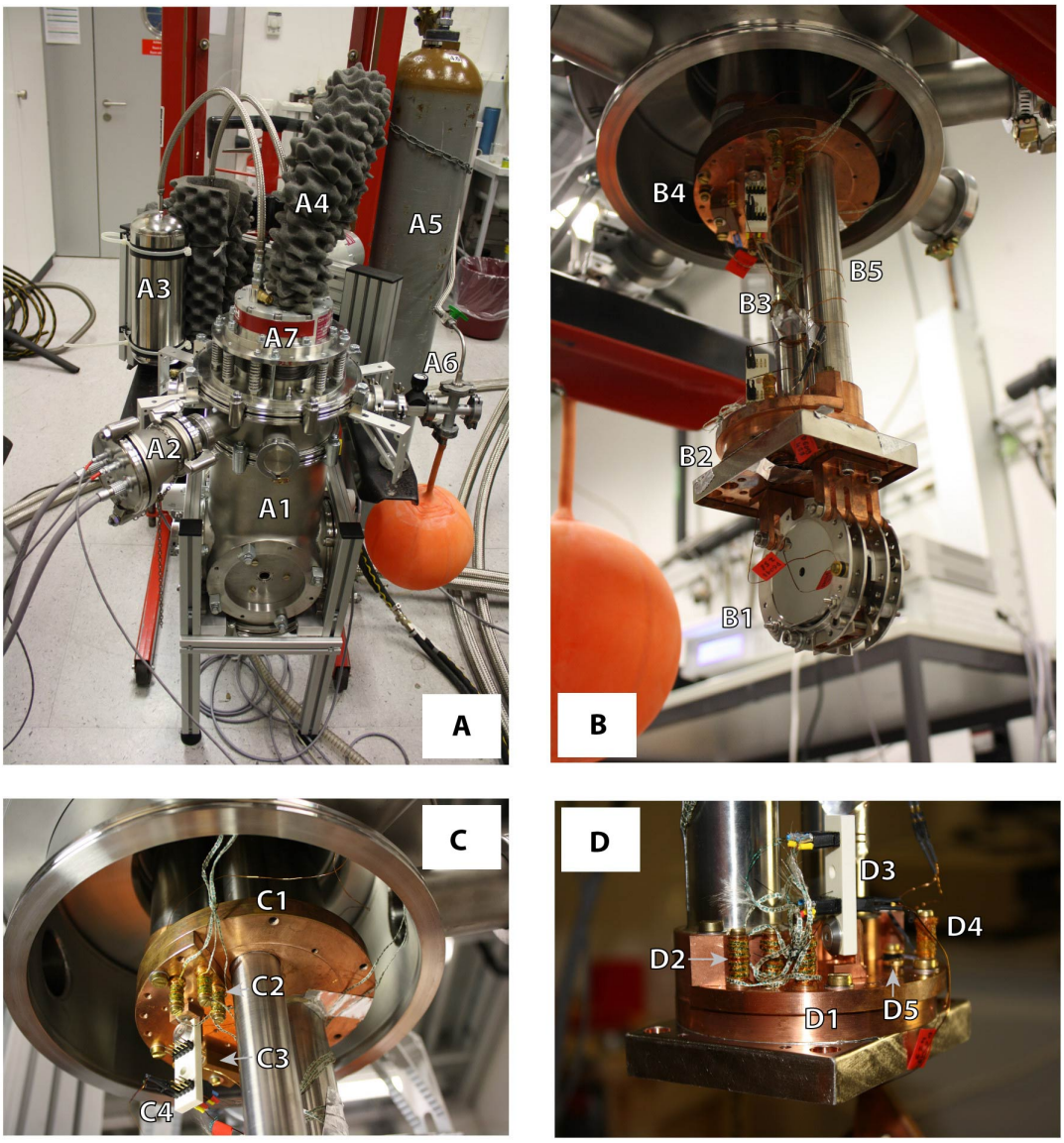

Figure 2.9: Pictures of the exterior and interior of the cryostat. A: The vacuum chamber seen from the outside. B: The pulse tube cooler and attached devices. C: Closeup view of stage 1. D: Closeup view of stage 2. A1: Vacuum chamber. A2: Temperature measurement system flange. A3: Reservoir(s) of the Pulse tube cooler. A4: Compressor hose. A5: Helium bottle. A6: Helium filled balloon and valve. A7: Pulse tube cooler heat exchanger. B1: Electrodes. B2: Pulse tube stage 2. B3: Pules tube 2. B4: Pulse tube stage 1. B5: Stage 2 part of regenerator. C1: Pulse tube stage 1. C2: Temperature sensor thermalizazions for stage 2 sensors . C3: Heaater 1. C4: Interconnection. D1: Pulse tube stage 2. D2: Temperature sensor thermalizations. D3: Interconnection. D4: Heater 2. D5: Temperature sensor.

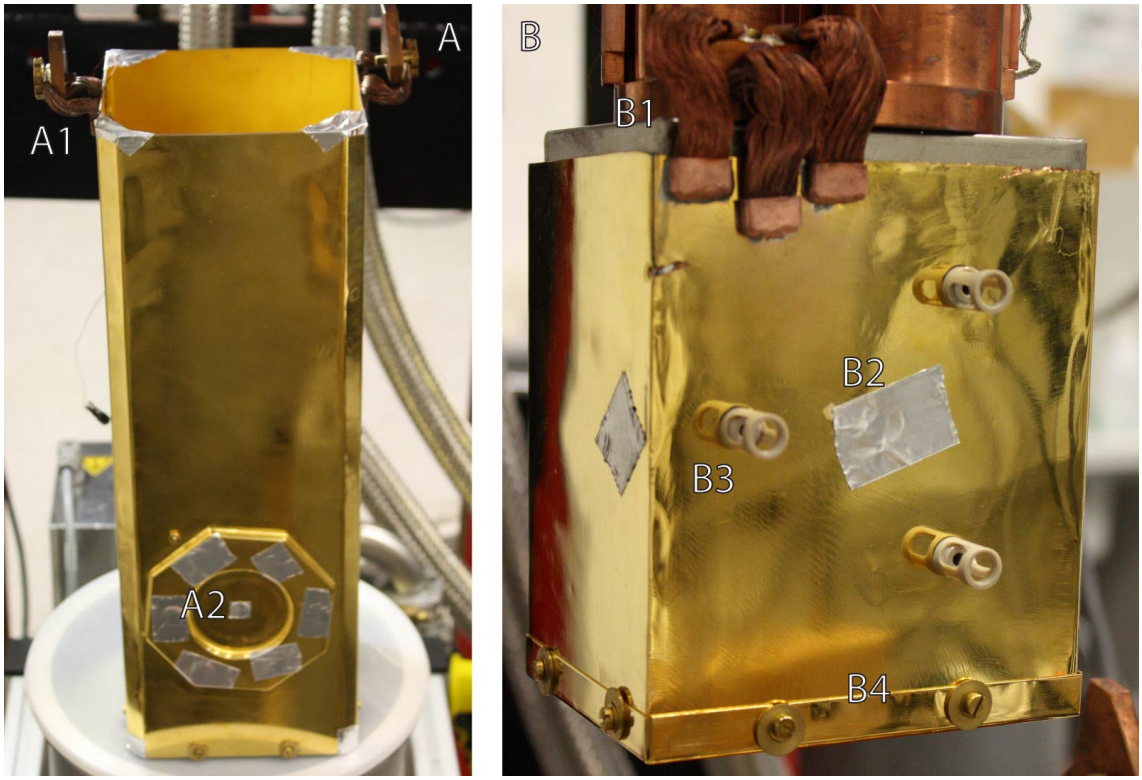

Figure 2.10: Stage 1 shield (A) and stage 2 shield (B). A1: Shield mount. A2: Taped skimmer hole in shield 1 (center). B1: Shield mount. B2: Taped skimmer hole in shield 2. B3: Plastic spacers. B4: Removable lid for electrode installation.

3 Temperature Measurement System

3.1 Introduction

Temperature control and monitoring is essential for the operation of a pulse tube cryostat. Therefore, a temperature measurement system was. With it the performance of the setup can be optimized from the beginning on and later the installed sensors will indicate if the setup behaves as expected. The operation at low temperatures is required by the superconducting microchip, used to suppress thermal excitations and to minimize black body radiation, a major source of decoherence in Rydberg atoms. Holes in the setup used for lasers and the atom beam make it more difficult to design and operate a pulse tube cryostat. This emphasizes the special importance of a good temperature measuring and control system and justify the increased effort and the care that has been taken in the design.

The following sections describe the hardware needed for the measurement and control system as well as the written software components for later analysis. Furthermore, the calibration of the temperature sensors was done and the performance of the pulse tube cooler while cooling to temperatures below 3K is determined. Several different setup configurations are tested to obtain information about the performance of the different components in order to further improve the setup.

3.2 Hardware

In the course of this thesis a temperature measurement system was designed and assembled. This requires the understanding of the involved devices like the sensors and the temperature controller. The cables from the temperature controller to the vacuum chamber and in its interior to the installed devices have been built. Additionally, a heater was constructed and all the parts have been assembled.

The following sections contain information about the measurement and working principle of the temperature sensors, the two heaters, considerations about the heat conduction along the installed cables and the thermalization of them at the pulse tube cooler stages. Additionally, a description of the temperature controller that reads out the temperature sensors and controls the heaters is given.

3.2.1 Temperature Sensors

To get information about a physical quantity in an experimental setup a device is needed to measure it. A physical effect in the sensor that depends non-ambiguously on the quantity to be measured enables the determination of the desired information.

To measure the temperature at various positions in the experimental setup the silicon diode sensors *LakeShore DT-670C-CU* are used. The key principle of the sensor is the temperature dependence of the forward voltage drop across a silicon p-n junction. This feature can be used in the large temperature range of 1.4K-500K.

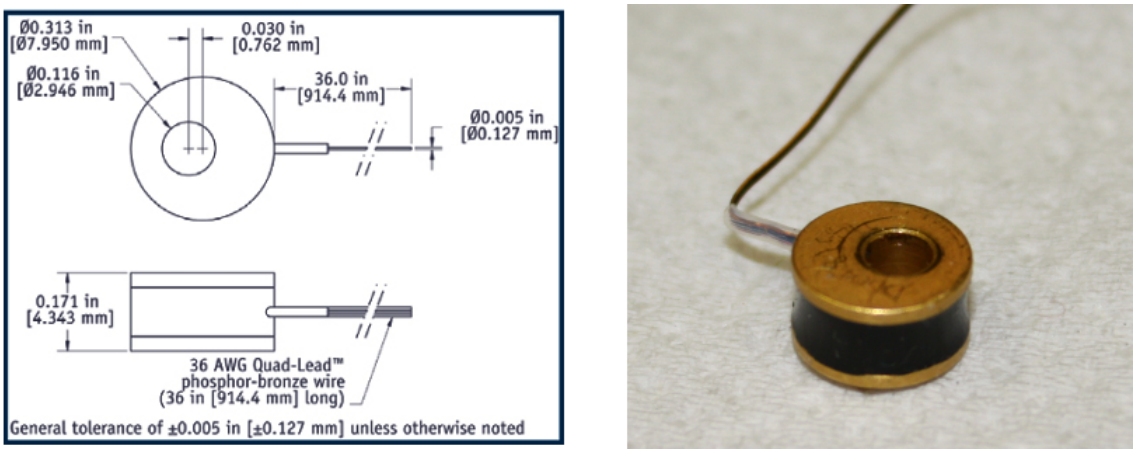

Figure 3.1: Copper package hosting the silicon diode inside.

The sensor is shown in Figure 3.1, its voltage drop and sensitivity in Figure 3.2. The diode is excited with a constant current of 10μA. Therefore, measuring 1V implies a resistance of 100kOhms. Measured voltages are on the order of 1V, which reduces measurement device complexity. At 4K the voltage is approximately 1.6V leading to a power dissipation in the sensor of 16μW. Despite this power being large in comparison with ordinary resistance thermometry the well designed package of the sensor and good thermal contact with the surrounding make self-heating negligible. The comparably large current was chosen by the manufacturer as a trade-off between self-heating and signal noise.

In Figure 3.2A the forward voltage drop is shown as a function of temperature. Three parts of the curve can be distinguished: the high temperature part from 500K to approximately 25K, the crossover in the vicinity of 25K and the low temperatures down to 1.4K. The average slope in the low temperature part is -22.6mV/K and in the high temperature part -2.1mV/K. Therefore the sensor is best suited for cryogenic temperatures since the sensitivity is largest there. Nevertheless the sensor can be used for use in the other temperature regimes, too.
The sensor behaves almost linear in the high temperature regime but for temperatures below the behavior is rather non-linear. In Figure 3.2B the derivative of the sensor voltage is shown. The almost linear and the non-linear regime can be clearly distinguished.

Explanation Of The Linear Behavior

The almost linear behavior in the high temperature regime is explained by considering that the silicon diode behaves like an ideal diode [29, p. 84ff.]. The assumptions are:

1) the charge density is a step function in the depletion layer,

2) outside the depletion layer the diode is neutral,

3) the Boltzmann relations for thermal equilibrium are also valid inside the depletion layer,

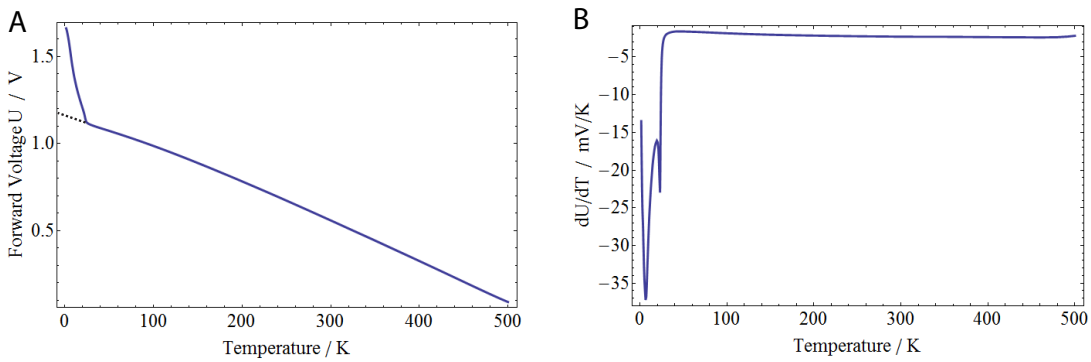

Figure 3.2: A: The solid line shows the forward voltage drop across the silicon p-n junction as a function of temperature. The dashed line shows the extrapolation of the almost linear high temperature regime to 0K. B: The derivative of A. It indicates the sensitivity of the sensor and that the high temperature regime is almost linear.

4) the injected minority carrier densities are small compared with the majority carrier densities and

5) currents are constant in the depletion layer.

Then the current-voltage characteristics is given by the Shockley equation

$$I = I_s(e^{eU/kT} - 1) \approx I_s e^{eU/kT}, \tag{3.1}$$

because $\mathrm{e}^{eU/kT} \gg 1$ in the temperature range used. The constant e in the exponent is the electric charge of a positive charge carrier, U denotes the forward voltage drop and k is the Boltzmann constant. I_s is the saturation current of the diode in the reverse direction. It is given as

$$I_s = T^{3+\gamma/2} e^{-E_g/kT} \approx C_1 e^{-E_g/kT} \tag{3.2}$$

for some constants γ and C_1. E_g is the bandgap of the diode material (Si) and is given by

$$E_g(T) = E_g(0) - \frac{\alpha T^2}{T + \beta}. \tag{3.3}$$

The current through the diode can then be written as

$$I = C_1 e^{-(E_g - eU)/kT}. \tag{3.4}$$

Since the current through the diode is held constant

$$(E_g - eU)/kT = C_2 \tag{3.5}$$

for a constant C_2 and finally the measured voltage

$$U = \frac{E_g - C_2 kT}{e}. \tag{3.6}$$

The change of E_g within a temperature range covering more than one order of magnitude, with constants α and β given in [29, p. 15], is

$$\frac{E_g(25K) - E_g(500K)}{E_g(500K)} = 0.097 \tag{3.7}$$

and thus small enough to be considered as negligible deviation from the linear behavior. Formula 3.6 indicates also the easy determination of the bandgap of silicon. Extrapolating the linear part to T=0 leads to $E_{g,extra}$(0K)=1.176eV, whereas literature [29, p. 15] provides a value of 1.170eV. The dashed line in Figure 3.2A indicates this extrapolation. The derivation seems to be consistent and the approximations well chosen.

The deviation from the linear behavior for temperatures below 25K is because of freezing out of free charge carriers to impurities in the diode base which increases the resistance and therewith the voltage [30].

The Advantage Of Four-Lead Measurements

To supply the diode with current and measure the forward voltage drop leads must be installed between the diode and the temperature controller. In principle the diode has only two ports: an electrically positive and a negative. Therefore it would be sufficient to use only two leads. However the leads for voltage measurement would be the same as the leads for current measurement. Therefore having a finite resistance R_{leads} produces a voltage drop of V_{leads}=IR_{leads} when the current I flows. The measured voltage V_2 between contacts V+ and V- from Figure 3.3A would then contain the voltage drop of the leads V_{leads} in addition to the forward voltage drop of the diode V_{diode}:

$$V_2 = V_{diode} + V_{leads}. \tag{3.8}$$

For a more precise measurement of the sensor the voltage and current leads are separated. This configuration is referred to as a *four-lead measurement*. Then the voltage drop in the current leads is not measured and the equivalent in the voltage leads is extremely small. This is because there will be practically no current flow in the voltage leads because the voltmeter has a comparably high resistance being parallel to the diode. This resistance can easily be on the order of $10^9\Omega$ or even higher compared to the diode resistance of approximately $10^5\Omega$. Therefore the additional voltage V_{leads} is negligible and the measured voltage is:

$$V_4 = V_{diode}. \tag{3.9}$$

3.2.2 Heaters

In addition to measuring the temperature it would be advantageous to stabilize it. The behavior of the setup would then be more reproducible. Therefore a feedback loop is needed. To change the temperature a heating element must be installed in addition to a temperature sensor. The amount of dissipated heat must be regulated by a temperature controller in

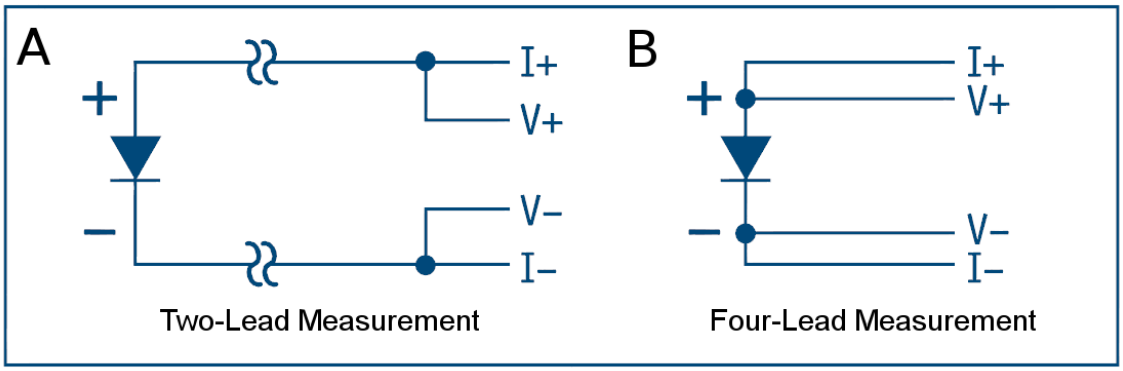

Figure 3.3: Comparison between two-lead (A) and four-lead (B) measurement schemes. In both sketches the silicon diode sensor is indicated on the left, the temperature controller that is responsible for current supply and voltage measurement is drawn on the right. Leads connect both devices. Figure taken from [31].

dependence on the measured temperature. The temperature controller is explained in more detail in Section 3.2.4.

The heaters used are simply electrical resistors, wires of a specific length, diameter and material that define the electrical resistance R_{heater}. Supplied with a voltage V and a current I the dissipated power is:

$$P_{heater} = IV = I^2 R_{heater} = \frac{V^2}{R_{heater}}. \tag{3.10}$$

The behavior of the pulse tube refrigeration system was tested with two heaters, one on each of its stages, see Figure 3.4.

Heater 1 is the *LakeShore HTR-25*, a cartridge heater with a precision-wound nickel-chromium resistance wire. The heater itself is a 25.4mm long cylinder put in a copper case for good thermal contact with the pulse tube stage. Its electrical resistance is 25Ω and the maximal approved power 25W.

Heater 2 is self-made. It consists of a Constantan wire, a copper-nickel alloy, wrapped around a copper cylinder. For enhanced thermal contact the wire is glued to the copper cylinder with GE 7031 varnish. Its electrical resistance is 55Ω. The maximal dissipated power should not overcome 3-5W because of the wire insulation.

3.2.3 Cabling And Thermalization

In order to reach the lowest temperature in the refrigerating system the cold parts have to be thermally isolated. Therefore, materials with low thermal conductivity are favorable. However, to connect devices from the interior to the exterior of the cryostat wires are needed. According to the Wiedemann-Franz law metals generally have good thermal conductivity in addition to good electrical conductivity. Therefore the electrical and thermal properties of the involved wires have to be well-considered. The parameters to be adjusted are the material itself, the length and the diameter of the cables.

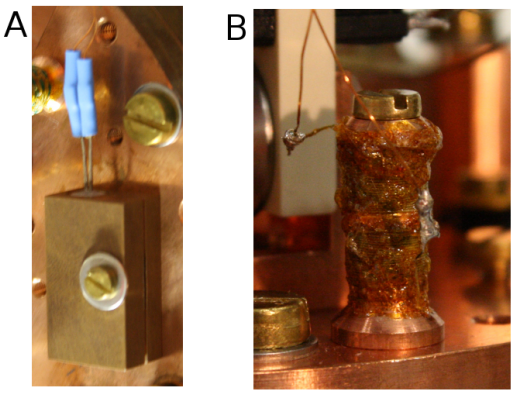

Figure 3.4: The two installed heaters. A: Heater 1 mounted on the stage 1. B: Heater 2 mounted on the stage 2. Both heaters are screwed to the corresponding pulse tube stage and are several cm long.

The heat flow $\dot{Q}$ (in units of Watt) through a homogeneous solid of cross-section A, thermal conductivity λ(T) and temperature gradient $\frac{\partial T}{\partial x}$ along a direction x is given by [32, p. 131] as:

$$\dot{Q} = \lambda(T) A \frac{\partial T}{\partial x}. \tag{3.11}$$

For a cylindrical wire with radius r and length l the cross-section is $A = \pi r^2$. The temperatures on the ends of the wire are T_1 and T_2. Integrating Equation (3.11) over the cable lengths gives:

$$\dot{Q} = \frac{\pi r^2}{l} \int_{T_1}^{T_2} \lambda(T) dT. \tag{3.12}$$

If the thermal conductivity is slowly varying with temperature in the range from T_l to T_h, one can approximate Equation (3.12) with:

$$\dot{Q} = \frac{\pi r^2}{l} \overline{\lambda}(T_l, T_h)(T_2 - T_1) \tag{3.13}$$

in the given temperature range with the average thermal conductivity

$$\overline{\lambda}(T_l, T_h) = \frac{1}{T_h - T_l} \int_{T_l}^{T_h} \lambda(T) dT. \tag{3.14}$$

From Equation (3.13) it is apparent that the minimum transferred power between the two temperature reservoirs is achieved when the radius r of the wire and the heat conductivity $\lambda(T)$ are small and the length l is big.

For the temperature measurement system copper and Constantan wires are used. According to [32, p. 133] the average heat conductivity in the range of 300K-4K is approximately 30 times higher in (electrolytic) copper than in Constantan. This indicates that Constantan will significantly reduce the heat conduction compared to copper. Also Constantan is used for the temperature sensor wires because the excitation current of 10μA is small and the dissipation of heat in the cables therefore negligible. For the heaters copper is the better choice because

the currents are larger and the heat should be dissipated in the heaters only and not in the cables connecting them to the outside. The diameters of the Constantan wires is 110μm and for copper 200μm.

To further decrease the thermal load on the cold part of the setup, cables must be thermalized at the different stages of the pulse tube cooler. This means that they are brought in good thermal contact with the pulse tube stages to cool the cables before reaching the connected device. These thermalizations avoid a direct thermal connection between the 300K surrounding of the vacuum chamber with the approximately 4K of the second stage or the sample holder with the superconducting microchip below the second stage. Since the cables for the temperature sensors at the second stage are thermalized successively at stages 1 (30K) and stage 2 (4K) of the pulse tube cooler the thermal load to devices at the second stage or the sample holder is significantly reduced. Technically, thermalization is done by winding the wires around a copper cylinder, gluing them with GE 7031 varnish to increase thermal conductivity between the wire and the copper and screwing the copper cylinder to the pulse tube stage. Figure 3.5 shows such a copper cylinder with a thermalized cable.

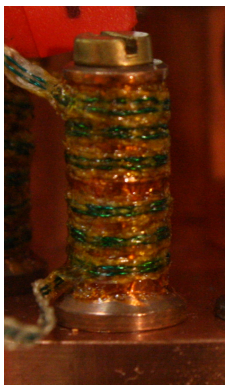

Figure 3.5: A Constantan cable (green) for temperature measurements is thermalized via the copper cylinder.

Since the heaters are connected with thermally well conducting copper wires, no thermalization is needed for heater 1 on stage 1. Heater 2 on stage 2 is only thermalized at stage 1.

3.2.4 Temperature Controller

The device for running the temperature sensors and the heaters is the *LakeShore Model 340 Temperature Controller*. A picture of the device is shown in Figure 3.6.
Two temperature sensors can be connected to standard sensor inputs (”11”) and additional eight via the installed input option card (”4”). For the temperature sensors the controller acts as a current source and a voltmeter. For the standard sensor inputs it measures the voltage at a rate of 50ms. The measurement rate for the additional eight inputs depends on the number of enabled sensors channels. The eight sensors are split such that there are two inputs with four sensors each. They work like the two standard inputs but the measurement rate of the input increases from 50ms with one sensor channel enabled to 400ms with all four

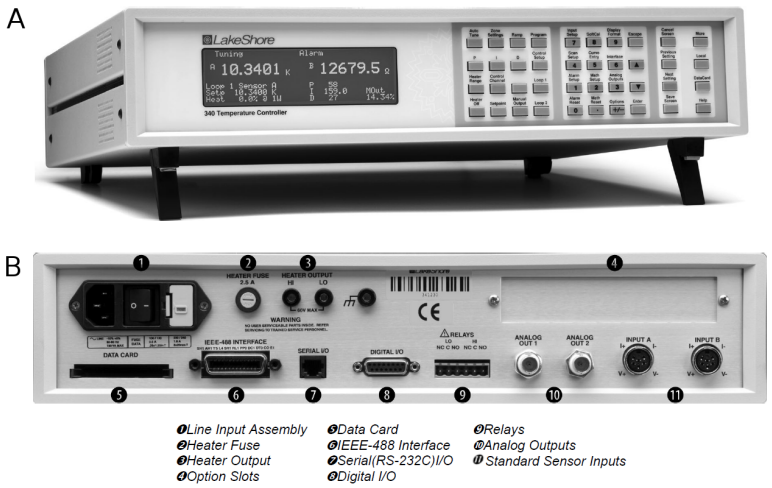

Figure 3.6: Overview of the temperature controller. A: Front view of the controller. B: Rear view of the device. The option slot ("4") is used for the *3468 Eight Channel Input Option Card* to measure up to 8 additional temperature sensors.

sensor channels enabled. After measuring the voltage it is digitized with a 24-bit analog-to-digital converter and translated to temperature with the corresponding calibration curve of the sensor.

Heaters can be connected to the heater output ("3") with a maximum power of 100W and to the analog output 2 ("10") with maximum power of 1W. Output "3" is a current source and "10" a voltage source. The device can control the temperature with two built in PID feedback loops. One heater and one temperature sensor are needed for one loop.

The cables to connect the temperature sensors and heaters are home-built. Information about them can be found in Appendices. For temperature sensor cables and the 100W-heater(heater on stage 1) the temperature controller provides shielding of the signal wires. Any two voltage, two current and two heater wires are twisted pairs and actively shielded by the controller. It applies a potential to the shields such that the voltage between the shield and the signal wires is minimal.

To control and readout the device a connection to a PC is made via the IEEE-488 ("6") GPIB interface.

3.3 Software

A software program has been written for taking data from the temperature controller and to allow for further analysis. Moreover, it is possible to control the heater output with the program.

The program is written in *National Instruments LabVIEW* because its graphical programming style provides a comparably fast and easy way of communicating with devices. Also it is

well supported from device manufacturers with instrument drivers which further simplifies programming.

The main task of the program is to read the temperature data from the temperature controller and writing it to a log file. This log file is then imported in *Wolfram Research Mathematica* for analysis and plotting. The program can also be relatively easy developed further to log other important quantities e.g. the pressure in the vacuum chamber. A connection from the pressure meter to the PC can be made via the RS-232 interface. Instrument drivers do exist, too.

Figure 3.7 shows a workflow diagram of the program. The program has an event structure. This means parts of the program will be executed when event sources like button clicks or timed loops, trigger the events. First is initialized the connection to the temperature controller, the log file is created and the registration of the possible events to the system. Event sources are timed loops that trigger the execution repeatedly at a rate T1 and T2 for events 1 and 2 and button clicks from the user for events 3 and 4.

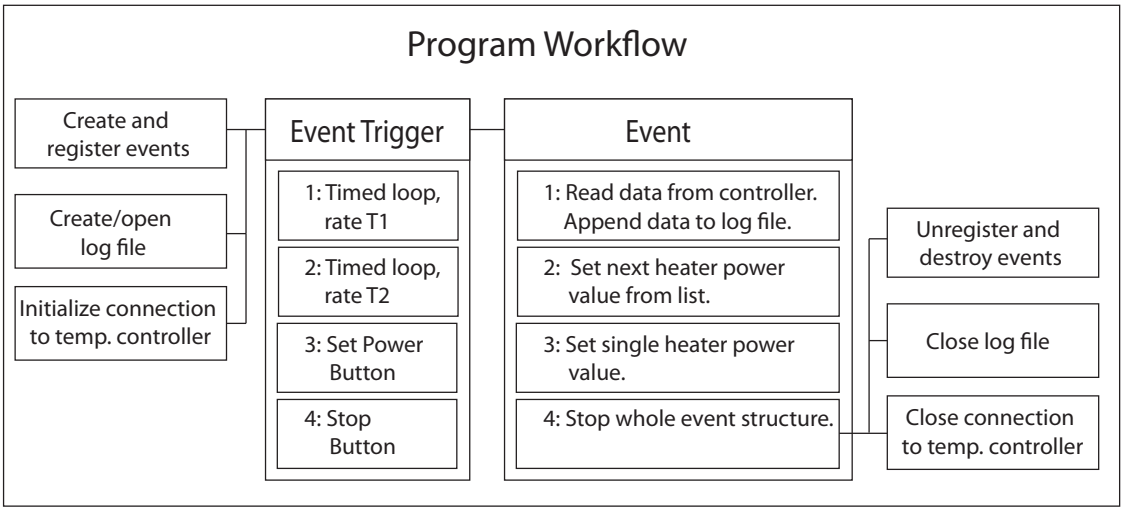

Figure 3.7: Overview about the structure of the program.

Event 1 reads voltage and temperature values of all sensors from the temperature controller. Depending on the user settings the values are overwritten with "-1" if logging of the sensor is unwanted. Afterwards, the data is appended to the log file together with a timestamp. The time has the format of seconds after 1st of January 1904. The reason why also the dummy values "-1" are saved is because it preserves the structure of the log file and makes further analysis easier. Repetition rate T1 is in principle arbitrary but is bounded from below by the the time the program needs to reed out all the sensors. This time is on the order of 500ms. For temperature logging purposes this does not constitute a restriction.

Event 2 sweeps the heater power from a predefined list of powers. This event was useful in the study of the behavior of the pulse tube cooler at different thermal loads. Results are shown in Section 3.4.3.

Event 3 sets only one heater power predetermined by the user.

Event 4 stops the execution of the events. Afterwards the connection to the temperature controller is closed, the log file is closed and the events will be unregistered from the system and destroyed. Then the program is finished.

It has to be mentioned that a considerable part of the program has been developed by Dr. Stefan Filipp.

3.4 Measurements

The following sections contain information about the cooling and warm-up behavior, the calibration of the temperature sensors, cooling times for various parts of the setup, the performance under thermal load and the behavior under several different setup configurations.

3.4.1 Cooling And Warm-Up Behavior Of Pulse Tube Stage 2

First measurements are performed with the calibrated sensor at the second stage of the pulse tube cooler. The stage was surrounded by the first stage shield. The temperature during cooling and warm-up can be seen in Figure 3.8. First the system is at room temperature (296K) and the pressure is reduced to about 10^{-7}mbar in the vacuum chamber. Cooling down to 2.8K needs roughly 60 minutes and is stopped after 93 minutes. Then the system warms up slowly due to heat transport through the pulse tube cooler and thermal radiation from the surrounding. In this measurement warm-up has been accelerated by inserting helium gas when the system has reached about 250K. The system needs 20h to reach this temperature. With the use of helium at the beginning of the warm-up and a pressure of 10^{-2}mbar the time for reaching 250K reduces to about 6h. Nevertheless using that amount of helium is not recommended because cooling of the vacuum chamber causes condensation of water on the outside of the chamber. A warm-up with an initial pressure of 10^{-3}mbar of helium or less will reduce the condensation of water to a minimum. The time to reach 250K will then be on the order of 10h. The slow warm-up of the system is used for calibrating the temperature sensors.

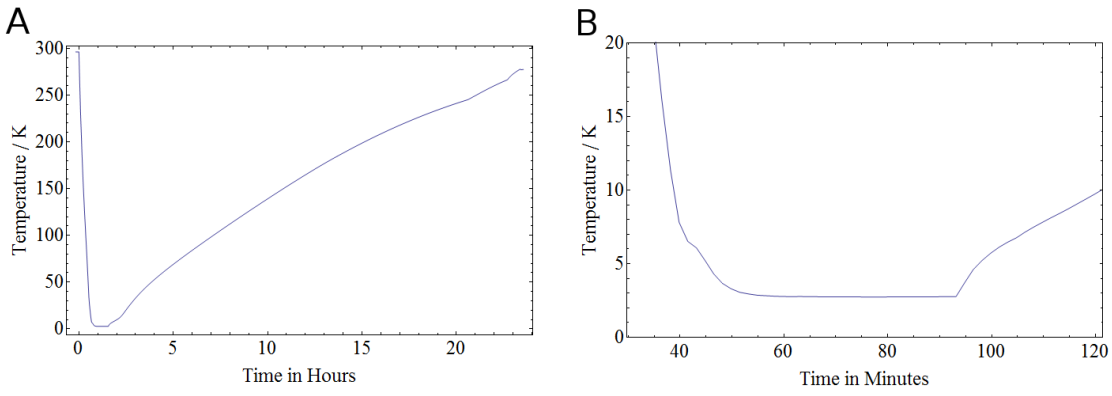

Figure 3.8: A: Time dependence of the second stage temperature while cooling and warm-up. B: A zoomed version of graph A. Time is relative to the start of cooling.

3.4.2 Calibration Of The Temperature Sensors

There are seven temperature sensors available for measurements. As has been mentioned above one of them was calibrated by the manufacturer. To obtain the temperature from the voltage measurements of the sensors a calibration curve must be installed on the temperature controller to convert between the two quantities. In principle there are three ways to obtain such a calibration curve.

First, one can use one standard curve for all sensors. This curve is provided by the manufacturer. Such a curve can be used because the reproducibility of the behavior of different silicon diode sensors is high. The given accuracy of the standard calibration curve used with the DT-670C-CU sensor is ±1K in the temperature range of 2K-305K.

Second, the so called SoftCal calibration can be used. The manufacturer measured data at two or three temperature reference points. For the two-point version this is the voltage of the sensor at 77.35K (liquid nitrogen) and 305K, for the three-point version a reference measurement at 4.2K (liquid helium) is made in addition. Then the SoftCal program fits a curve through these data points. For the three-point calibration the errors at temperatures below 10K are on the order of ±0.5K. Errors decrease to approximately ±0.15K for temperatures up to 305K.

Third, every sensor is individually calibrated over the whole temperature range. Since with the help of the LabVIEW software it is possible to log temperature and voltage of all sensors they can be calibrated individually. This method has been chosen for calibration of the sensors because it improves the accuracy in comparison to the other two methods. For an overview about the setup for this calibration method see Figure 3.9. The already calibrated sensor is

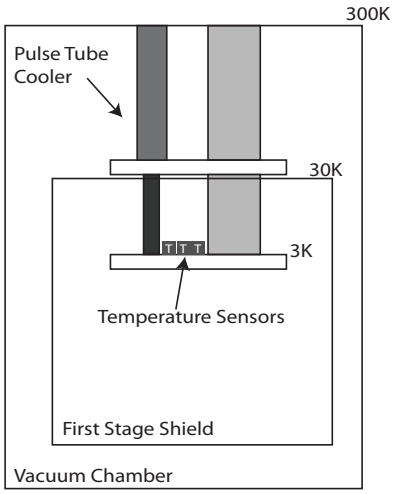

Figure 3.9: Experimental setup for the individual calibration of the temperature sensors over the whole temperature range.

placed on the second stage of the pulse tube cooler which reaches a temperature of about 3K. Next to the calibrated sensor two uncalibrated sensors are placed. They are screwed on a common copper plate and are approximately 2cm apart from each other. Because letting

warm up the system from 3K to room temperature takes roughly 10h-20h the temperature gradients in the copper plate should be small. Since the sensors are placed close to each other it is assumed that the temperature gradients are negligible.

During warm-up the temperature range of approximately 3K-290K is covered and within this range the temperature of the calibrated sensor is correlated with the measured voltage of the other two uncalibrated sensors. Afterwards a calibration file is created for each sensor from the measured data and installed on the temperature controller. At the low or high temperature end the data has been extrapolated to avoid the controller to be out of range. At the high temperature end a linear function from 290K-370K and on the low temperature end from 3K to 2K a polynomial up to second order has been used. See figure 3.10. The dots are the "breakpoint table" used by the instrument for conversion between voltage and temperature. The dots are inhomogeneously distributed over the temperature range. Dot density has been chosen to be three times higher below 30K because these temperatures are the most important for the experiment. Also the sensor behaves non-linearly in this region. The region of larger dot density covers the crossover region, too.

This method has been applied to all six uncalibrated sensors.

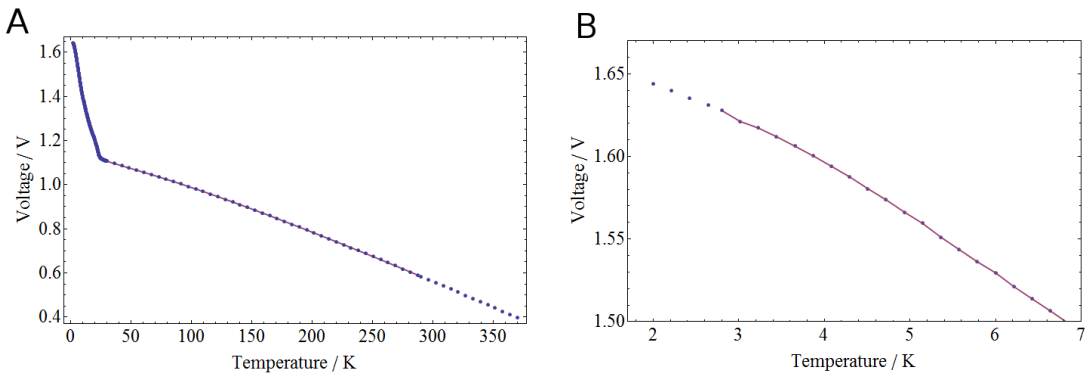

Figure 3.10: A: Typical calibration data. The solid purple line covers the measured data. Blue dots are the actual calibration data feed into the temperature controller. Both extrapolations are clearly observable. B: Zoomed version of graph A.

To determine the quality of the calibration method the temperature of the sensors is recorded while the setup was allowed to warm up a second time. The quantity of interest is the difference of the temperature to the calibrated sensor in dependence on the measured temperature of the uncalibrated one. This data is shown in Figure 3.11 and Table 3.1. The maximal uncertainty of the calibrated sensor was measured by the manufacturer and is 34mK for temperatures up to 300K. This value has to be added to the maximal temperature difference of the sensor (Table 3.1) to state the total temperature uncertainty. Combining these two numbers it can be seen that this method is approximately as good as the SoftCal calibration method (500mK) or is even better. The maximum temperature difference occurs shortly after the pulse tube cooler has been turned off at about 3K-5K. This feature is an artifact of the measurement procedure.

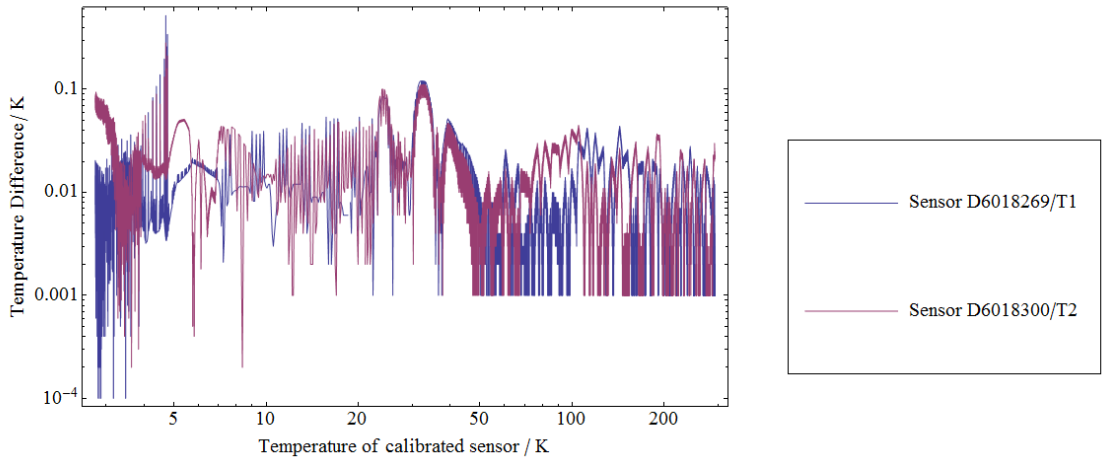

Figure 3.11: Difference of measured temperature for two selected uncalibrated sensors relative to the calibrated sensor. Plotted is the absolute value of the difference. Note the log-log scale.

Sensor Name	Avg. Temp. Difference / mK	Max. Temp. Difference / mK
D6017132	15.0	133
D6018258	16.6	149
D6018269	9.20	521
D6018299	47.7	284
D6018300	11.5	284
D6018301	17.4	142

Table 3.1: Sensor characteristics based on the test run. Values are relative to the calibrated sensor.

3.4.3 Characterization Of The Experimental Setup

Cooling Performance For The Total Setup

With calibrated temperature sensors the setup can be characterized at various positions simultaneously. This is necessary because for optimal operation the performance of the setup has to be checked carefully at least once in the beginning of the assembly. Of interest are here the steady state temperatures and the cooling times of the two heat shields, the electrode stack as well as the two pulse tube stages, see Figure 3.12.
With this configuration the setup has been cooled to an equilibrium state, see Figure 3.13.
The cooling of pulse tube stage 2 and the attached heat shield is very fast in the first hour, Figure 3.13A. In Figure 3.13B it is shown that it takes approximately 2 hours for the shield to reach a stable temperature, The stage takes roughly 15 minutes more than the shield to equilibrate.
Note also that the stage 2 is colder than the final stable temperature for half an hour. This is related to the temperature of the first stage. A warmer first stage can cause more gas flow to the second stage and increases the cooling effect. After approximately 2 hours and 15 minutes the first stage reaches equilibrium and the temperature at the second stage rises again.
The stage 1 shield reaches the equilibrium temperature approximately after 2 hours.

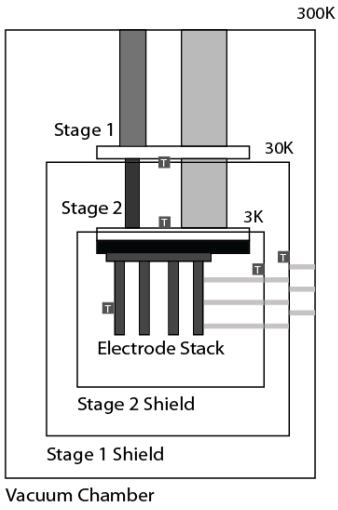

Figure 3.12: Schematic setup for the test of cooling times and equilibrium temperatures. Installed temperature sensors are marked with a "T".

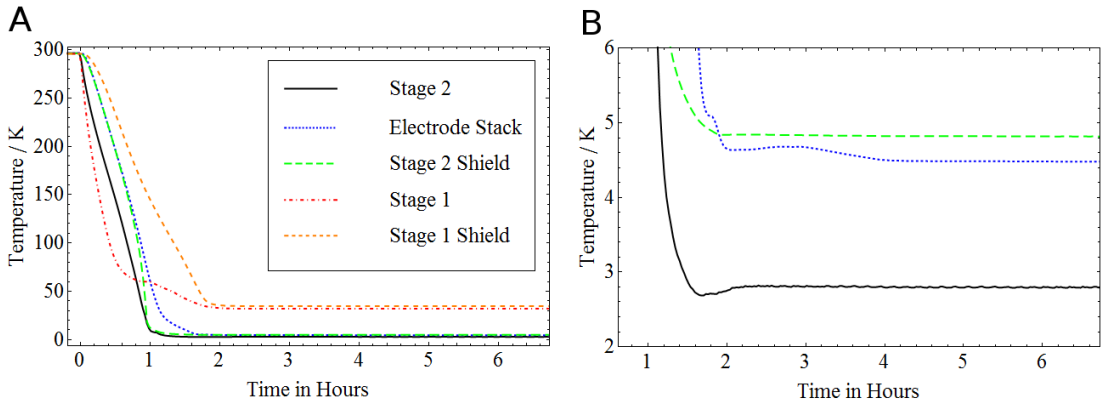

Figure 3.13: A: Cooling performance of the setup at five different positions. Time is relative to the start of cooling. B: Zoomed version of graph A to observe the performance of stage 2 and connected parts at low temperatures.

The electrode stack cools fast in the first hour, too. Afterwards the cooling speed is reduced. Until hour 2 the temperature drops continuously. As can be seen in Figure 3.13B a stable temperature at all positions is achieved only after four hours.

For the electrode stack it has to be mentioned that the electrodes are made from stainless steel. They are interconnected with electrically insulating spacers made of Shapal-M with comparably large heat conductivity at room temperature. However it turned out that the Shapal-M material for the spacers used initially has not enough thermal conductivity at low temperatures. Therefore, the electrodes used for this test experiment are interconnected with copper spacers because they conduct thermally very well at low temperatures, a viable strategy to test the heat load in the electrodes. For final operation the copper spacers must be exchanged with an appropriate material. Future tests will use sapphire spacers and it is also intended to test new electrodes made from aluminum for better thermal conductivity. A comparison of copper and Shapal-M spacers used with the electrodes is done in Section 3.4.3, Figure 3.17.

Pulse Tube Characterization

In the previous Section it has been determined that the setup can reach a thermal equilibrium and how long the different parts need to arrive at this state. This section is devoted to the performance of the pulse tube in comparison to its specified performance. From the measured data and the temperatures for different setup configurations the incident heat load can be estimated and compared to calculations.

The experimental setup for the test of the pulse tube cooler is shown in Figure 3.14. It consists of the stage 1 shield, two temperature sensors ("T") and two heaters("H") on the stages.

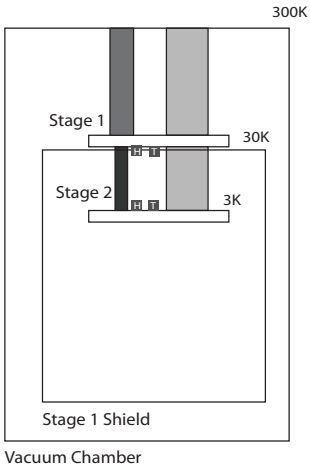

Figure 3.14: Diagram of the experimental setup for the test of the pulse tube cooler performance.

The idea behind this setup is to expose the stages to a predefined thermal load with the two installed heaters described in hardware section 3.2.2. The temperatures of the stages change and the equilibrium temperature is recorded. The obtained data is shown in Figures 3.15 and 3.16.
On the stage where the heaters are installed, the temperature increases when the heater puts more thermal load on the stage, see Figure 3.15A and C.
Figure 3.15B shows the weak dependence of stage 2 temperature on the power of heater 1. The trend shows a decrease in temperature for more heat load on stage 2. The change is approximately -0.1K for 25W heater power, the temperature decreases from 2.8K to 2.7K. This effect has been mentioned before and is a result of a better gas flow towards stage 2 which increases the cooling power at this stage. The effect vanishes for higher thermal loads on stage 2. Then the temperature of stage 1 is only dependent on stage 1 heater power.
Graph D shows the influence of heater 2 on stage 1 temperature. The higher the power the higher the temperature. The effect is increasing for higher heater 1 powers, too. The reason for the kink at 0.25W heater 2 power is not known.

The same data is plotted and compared to the manufacturer data in Figure 3.16.

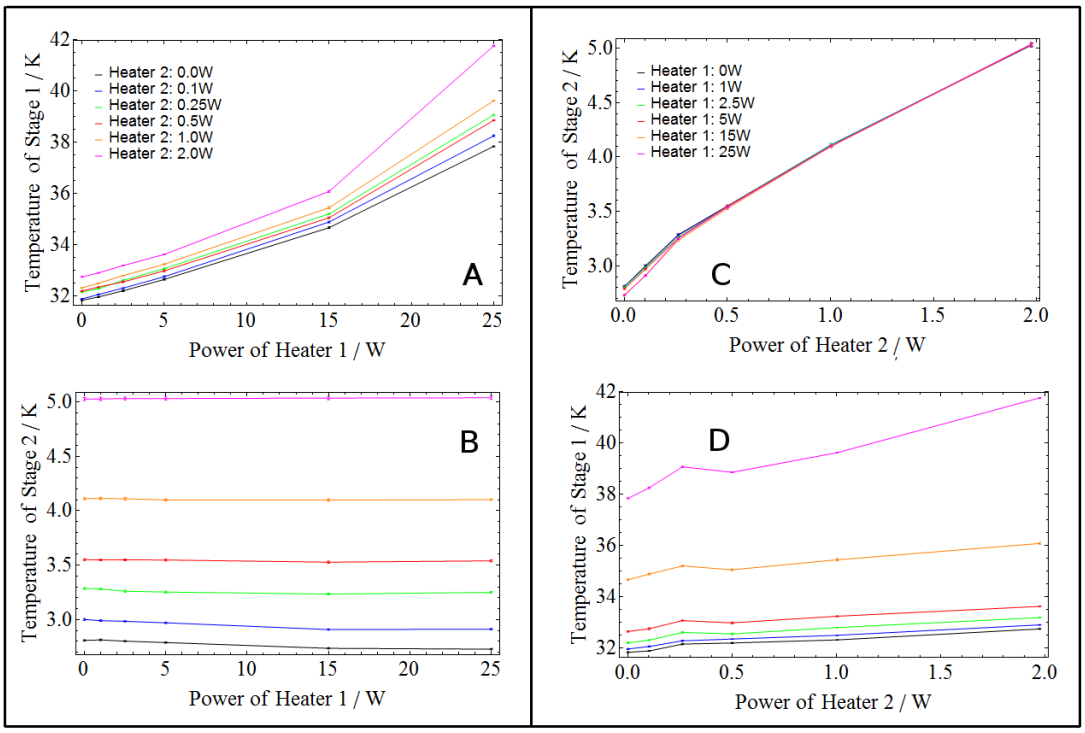

Figure 3.15: Obtained power dependent equilibrium temperatures of the pulse tube stages. Graphs A and B show the heater 1 power dependence of the temperatures of both stages for constant heater 2 powers. Graphs C and D the same for heater 2 power dependence for constant heater 1 powers.

Vertical lines in the figure are lines of constant heater 1 power. Nearly horizontal lines are lines of constant heater 2 power. The manufacturer used heaters up to 36W for heater 1 and up to 1.35W for heater 2. Provided are only four data points.

The measured and expected performances match well. Comparing the 0W-lines a positive temperature shift is observable. A positive shift means more thermal load incident on the stages. It is assumed that this is a result of imperfect shielding and maybe due to heat transport from the installed wires.

The shifts of the measured data relative to the manufacturer data for the horizontal 0W-line from heater 1 are between 0.06K to 0.12K. Assuming a linear behavior between the four data points measured by the manufacturer, this corresponds to 0.05-0.1W and 0.08W average. For the vertical 0W-line from heater 2 the shifts are 0.13K-0.53K, correspond to 0.41W-1.59W and average power shift of 1.11W.

Another comparison can be made with the 1W horizontal line of heater 2. Linearly interpolating the original data would give a temperature on the second stage of about 3.9K. Measured data with subtracted offset indicates a temperature of 4.0K. Therefore the obtained data seems to be in good agreement with the expected performance and can be used to determine heat loads for different setup configurations.

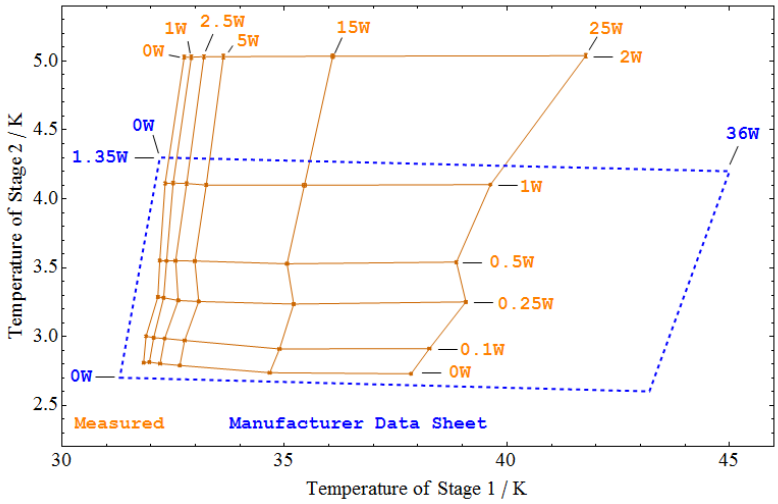

Figure 3.16: "Capacity curve" of the pulse tube system reflecting its cooling performance. Horizontal lines are lines of constant heater 2 power and vertical lines the analog for constant heater 1 power. Details are explained in the text.

Temperature Distribution For Different Setups

For the analysis so far the setup has been operated with shields where the holes are closed. In the further analysis they will also be opened to find out how the temperatures change when the setup is in a more realistic configuration.

From the various tested setup configurations only the most important for the experiment are shown in Figure 3.17.
Figure 3.17A shows the configuration without electrodes and shields installed, Setup 01. The stages are exposed to the thermal radiation from the vacuum chamber, about 300K. Because no shielding is used, the temperatures of 32.5K for stage 1 and 5.1K for stage 2 are the maximum temperatures for the stages.

Next, two heat shields are installed together with plastic spacers, see Figure 3.17B - Setup 05. The spacers are needed to fix the position of the shields and therewith the position of the holes in the shields relative to the vacuum chamber. Compared with Setup 01 the stages are colder with the installed shields as expected. The shields, however, are both warmer than the stages through which they are cooled. Shield 1 is 3.2K warmer than its stage and shield 2 3.1K.
Additionally a temperature difference to the stage of +2.8K was measured for shield 1 without using spacers and 2.2K for shield 2. The setup configurations were like Setup 05 but without spacers. We can conclude that the major part of the temperature difference of the shield to the corresponding stage is not from thermal conduction through the spacers. Therefore the heat conduction of the shield and the shield mount to the stage is mostly responsible for the temperature difference of shield and stage.

When the electrodes and their spacers were installed in addition to Setup 05 an electrode temperature of 4.3K was measured, see Figure 3.17C - Setup 08. This is reasonably low

	Stage 1	Stage 1 Shield	Stage 2	Stage 2 Shield	Electrodes
Setup 01	32.5K	-	5.1K	-	-
Setup 05	31.8K	35.0K	2.8K	5.9K	-
Setup 08	31.8K	35.2K	2.8K	5.2K	4.3K
Setup 10	32.0K	35.0K	3.2K	8.0K	11.9K
Setup 11	32.0K	35.1K	3.2K	10.9K	27.8K
Setup 12	31.9K	35.1K	3.0K	9.3K	16.0K

Table 3.2: Temperatures in the cryostat for various setups. The values are the same as in Figure 3.17

but slightly warmer than the stage with 2.8K. The electrode material is stainless steel and the connection between the electrodes is made of copper spacers. These spacers simulate a material with high thermal conductivity and must be replaced when the electrodes are used later. The temperature of the stages is unchanged but a significant decrease of -0.7K happens for the shield 2 to 5.2K. The shield seems to be cooled via the spacers and the electrodes.

In Setup 10, Figure 3.17D, the change to Setup 08 consists of opening several holes with circular area in the shields. The holes are the micro-channel plate holes (MCP) on the left where the atoms get detected. On the bottom, holes for a screw to change the distance between sample holder and atom beam are placed. Furthermore, there is an entry holes for the atom beam, called the skimmer hole. Also a hole for the laser to excite the atoms to Rydberg states was opened. The diameters of the holes are listed in Table 3.3. In presence of these holes an increase of +0.4K to 3.2K on stage 2 and of +0.2K to 32K on stage 1 is observed. More significant are the temperature changes on the electrodes with +7.6K to 11.9K and on shield 2 with +2.8K to 8K. With only the MCP holes open, the final temperatures are only slightly lower because the MCP holes are big in comparison to the other holes.

Hole	Diameter (Shield 1)	Diameter (Shield 2)
Skimmer hole	8mm	8mm
MCP hole, original	40mm	30mm
MCP hole, reduced	20mm	20mm
Screw hole	6.5mm	6.5mm
Laser hole	5mm	6mm

Table 3.3: Various holes in the shielding.

The change in Setup 11, Figure 3.17E, to the previous is the use of the originally designed electrodes to make a comparison to the thermally well conducting copper spacer version. Here the electrodes are also made from stainless steel but the spacers are now made from Shapal-M ceramics. This material was intended to be used because it is electrically insulating but thermally well conducting at room temperature. The temperature of the electrodes rose to 27.8K and the shield 2 to 10.9K. Since for the superconducting microchip temperatures of about 5K are required, electrodes with 27.8K temperature in its vicinity are inappropriate. Therefore the setup and/or the electrodes have to be modified.

The Setup 12, Figure 3.17F, reduces the diameter of the MCP holes to 2cm each. The effect on the electrode temperature decreasing from 27.8K to 16.0K is significant. Also shield 2 and the pulse tube stages have slightly reduced temperatures.

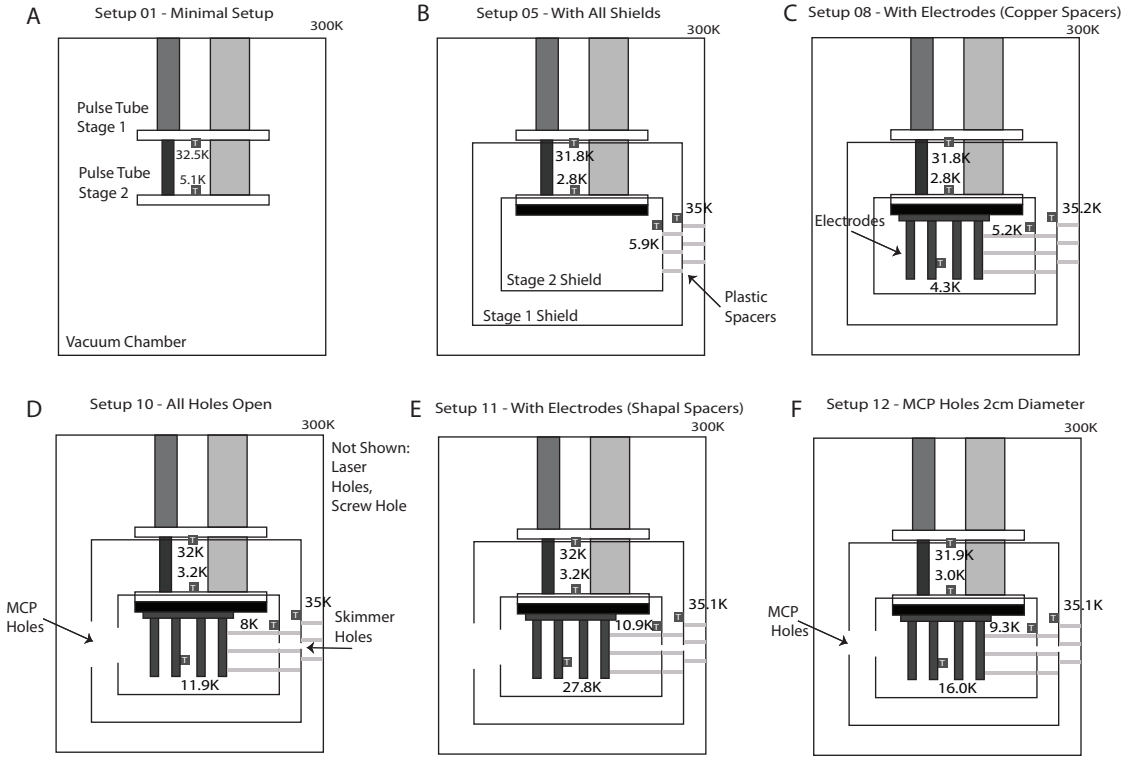

Figure 3.17: Different tested setup configurations. Starting with an empty configuration (A), shields and spacers are added (B). Then the electrodes are installed (C) and all holes are opened (D). The spacers in between the electrodes are changed from copper to Shapal-M (E) and the MCP holes were reduced in size (F).

3.5 Results And Conclusions

Additionally to the direct results from the measurements before, with the measured temperature distribution data from Section 3.4.3 one can obtain the corresponding incident powers from Figure 3.16. The result can be seen in Table 3.4.

Setup	Configuration	Stage 2 Temperature	Stage 2 Power
01	No shields	5.1K	2.05W
05/08	All shields / and electrodes	2.8K	0W
10/11	MCP hole 3cm diam.	3.2K	0.21W
12	MCP hole 2cm diam.	3.0K	0.10W

Table 3.4: Obtained powers incident on stage 2 for different setup configurations.

The incident power can be approximated from the Stefan-Boltzmann law by treating all shield 2 holes as 295K blackbody radiators:

$$P_{bb} = A\epsilon\sigma T^4 = \pi \sum_{i=1}^{4} \frac{d_i^2}{4} \sigma T^4, \tag{3.15}$$

where P_{bb} is the totally emitted blackbody radiation from the holes in units of power. A is the surface area of the blackbody emitter and σ is the Stefan-Boltzmann constant. ϵ is the emissivity and reflects the ability of a body to emit radiation relative to a black body. Here ϵ=1 since we assume blackbody radiators. The d_i are the diameters of the 4 holes in the stage 2 shield.

We obtain a total incident power of 0.35W which is on the same order of magnitude as the determined 0.21W in Setup 10 and 11. Since the metallic shields and stages do not absorb all of the power, radiation will be reflected and the total absorbed power should be lower than the calculated power. Therefore, the difference between the calculated and measured powers should be even smaller than estimated here.

In summary, the temperaturse of the pulse tube stages, the heat shields and the electrode stack were determined under different setup configurations. Since the sample containing the superconducting microchip will be at least partly cooled via the electrodes this temperature is the most relevant. Also, because the electrodes are in the vicinity of the sample and would heat it up due to blackbody radiation. It has been determined that even under so far ideal conditions from Setup 10 with thermally well conducting copper spacers between the electrodes the temperature of 11.9K of the electrodes is too high. With Shapal-M spacers, the temperature rose even to 27.8K. The reduced size of the MCP holes to still 2cm diameter had a significant effect, but with 16K electrode temperature improvements are necessary.

3.6 Suggestions

During writing the thesis, the setup has been improved. The electrodes are now made from aluminum and are coated with copper and gold. The spacers in between the electrodes are now made from aluminum oxide. The geometry of the MCP hole has also been changed to a hollow cylinder and the hole is reduced further. This leads to an electrode temperature of 4.3K and stage 2 temperature of 3.2K. A further reduction of the electrode temperature might be possible with sapphire spacers [33, p. 66].

The interesting idea which arose from discussions of coating the shields on the inside such that they absorb radiation that entered the shields and make them as reflective as possible on the outside might be worth to get implemented.

Also using a material with a higher critical temperature T_c for the superconductivity of the microchip material could allow for studies of the interaction between atoms and superconducting surfaces.

3.7 Summary

The previous considerations show that a temperature measurement and control system could be successfully planned, assembled, installed, calibrated and used to characterize the experimental setup.

The cooling and warm-up measurements of the setup have shown that reaching stable low temperatures takes approximately 2h. For the electrodes this can extend up to 4h. Warm-up to 250K needs 10h to 20h depending on the amount of helium gas used to increase the heat exchange between the hot and cold parts.

The calibration procedure yields average temperature differences to the calibrated sensor between 9.20mK and 47.7mK and maximum differences between 133mK and 521mK. The chosen calibration method is at least as good for calibration as the best standard method SoftCal.

The measured behavior of the pulse tube cooler system indicates that it performs according to the manufacturer specifications. By taking more data points than the manufacturer a better evaluation of the performance was possible. A slight offset in temperature compared to the provided data shows that the system is exposed to a thermal load already. The average power shift relative to the manufacturer data are +1.11W for stage 1 and +0.08W for stage 2. The sources are assumed to be imperfections in the shielding. Estimates for the heat conduction through the installed wires could only explain $\leq$5 percent of the obtained incident powers. The incident heat loads on pulse tube stage 2 were determined as 0.21W with the MCP holes of 3cm diameter and 0.10W for 2cm diameter.

The temperature of the electrodes was determined in different configurations. The result was that the heat conduction of the electrodes is too small and the incident thermal load to the setup too large for the planned experiments. Therefore suggestions were made to improve the experimental setup and are partly implemented already. With the implemented changes the temperature of the electrodes could be reduced to 4.3K.

4 Vibration Measurement System

4.1 Introduction

The motivation of dealing with vibrations are the quantification of them in the current experimental setup because they will induce time-dependent fields as seen from the atom's moving frame of reference. Therefore we first deal with the nature of vibrations in the introductory part and what their implications are on the experiment. In Section 4.2 the setup for measuring the vibrations will be explained in detail. Section 4.3 describes the calibration of the sensor as well as the signal conversion to and between mechanical quantities like acceleration, velocity and displacement. Vibration measurements in different buildings are compared to find the potentially best place for the experiment and these sites are characterized over days to observe the variations in the vibrations over time. Finally vibrations inside the cryostat with the vacuum chamber and the pulse tube cooler are measured.

4.1.1 What Are Vibrations?

Vibrations are generally a dynamical mechanic excitation that may cause a dynamic response of a physical system [34, p. 1.1ff.]. In opposition to a shock, a vibration is a dynamic excitation with a relatively long duration as compared to the time required for a physical system exposed to that excitation to fully respond. The description of that excitation is basically given by the excitation magnitude as a function of time, called the time history.
Broad classification of vibrations can be made in deterministic type and random type. Deterministic excitations have the property that their future time history can be predicted with only minor errors. The prediction may be based on analytical calculations from fundamental physical knowledge about the system or by repeated observation of the excitation under identical circumstances. Random excitations do not allow to predict the future time history of the vibration based on analytical calculations or previous observations of the system.
Additionally the vibrations can be stationary or non-stationary. Stationary means that basic properties like average value and variance do not vary with time. This is often the case when the circumstances that lead to the vibration are time invariant. Non-stationary vibrations on the other hand have basic properties that vary slowly in time relative to the lowest frequency of the vibration.
In general vibrations are of mixed type such that they will contain deterministic and random components but typically one of them will dominate.

4.1.2 Vibration Sources

According to the above a vibration source is anything that produces a dynamical mechanic excitation.

In buildings these can be for instance industrial, transportation, construction and domestic noise [35]. But also natural and human sources might be worth taking into account.
Industrial noise is caused often from mechanized industry and their mechanical equipment. Transportation noise is caused by road, rail and air traffic. Construction noise from machines like cranes and cement mixers as well as from hammering, boring and other work processes. Domestic noise from mechanical devices like heat pumps and ventilation systems but also from voices. Sound from fans and humming of transformers are also often encountered in laboratories. In the experimental setup the operation of vacuum pumps and the pulse tube cooler should be the major sources of vibrations. Natural sources would contain for instance earth quakes, wind and rain.

4.1.3 Influences On Experiments

Vibrations will induce a displacement between rigid parts and movable parts of the setup in an uncontrollable way. In the planned experiments, atoms are supposed to fly over tiny structures on a microchip. The interaction of the atoms with the electric fields from the on-chip guide and from the microwave resonator depends on the distance of the atoms to the microchip. Therefore, vibrations would change the interaction strength of the atoms and the electric fields, thus complicating precise control over the atoms with DC and microwaves fields. The changing field strengths at the atom's positions caused by vibrations create different experimental results. In the detection the average is taken over these different results.
Also the interaction with the electric fields for the ionization of the atoms are changed, when parts of the experiment are vibrating. This influences which atoms will be ionized and thus has implications on the detection process and the precision of the control over the atoms.

4.2 Hardware

In this section an overview about the involved devices for the vibration measurements is given. Afterwards the vibration sensor will be explained and how the obtained voltage signal is transformed into information about the movement of the sensor.

4.2.1 Overview About The Setup

A photograph of the setup is shown in Figure 4.1, the signal path is depicted in Figure 4.2. In the geophone sensor vibrations induce a voltage between the two signal leads. Via a twisted shielded cable the signal reaches the signal conditioner where the signal is amplified and bandpass filtered. Then the signal is converted from analog to digital (ADC). Finally the digital voltage signal is converted to the desired type of spectrum: acceleration, velocity or displacement for further analysis and storage.

4.2.2 Cable Shielding

In order to prevent too much noise in the signal it is advantageous to shield the signal leads from the geophone to the voltage preamplifier. A metallic case around the leads acts as a Faraday cage and prevent the signal leads from electrical noise. The twist of the two signal

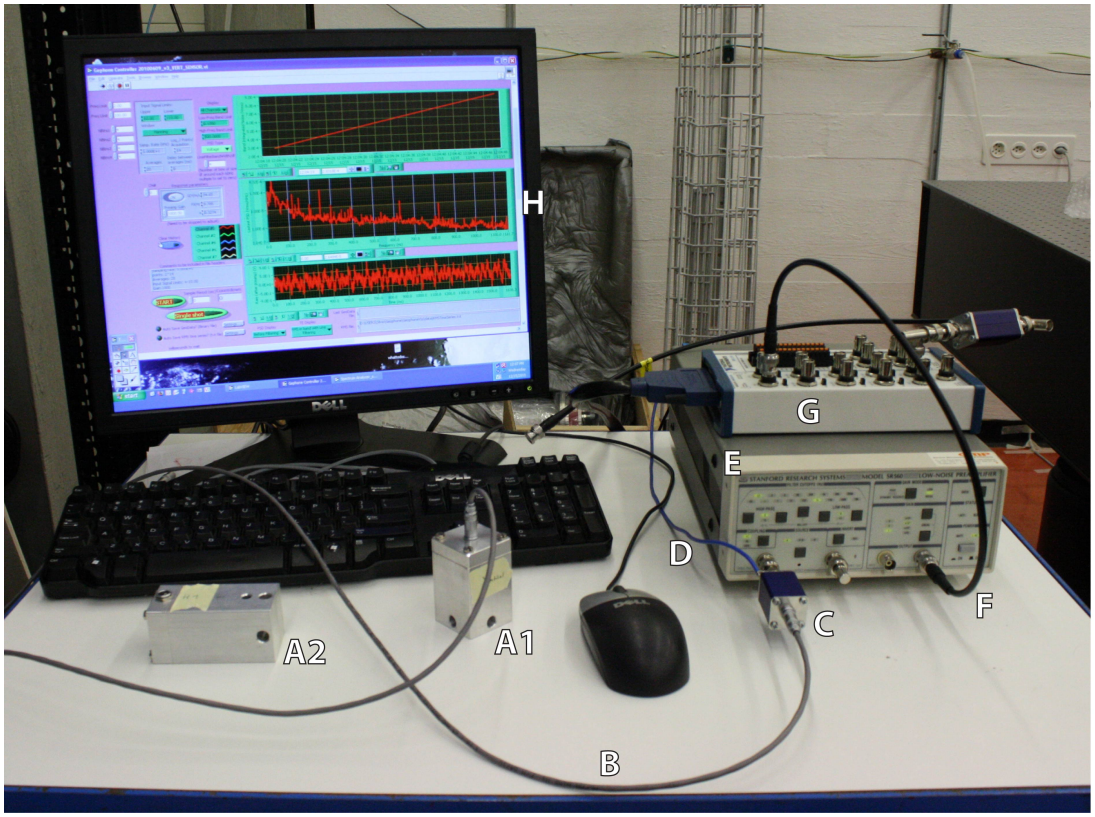

Figure 4.1: Photograph of the geophone hardware. A1 & A2: Vertical and horizontal geophone. B: Twisted shielded cable with Lemo connectors. C: SUCOBOX adapter to convert Lemo to BNC. D: Shield grounding connection. E: SR560 voltage preamplifier. F: Amplified signal output. G: Data acquisition system and ADC. H: Spectrum.

leads reduces voltages by time-dependent magnetic fields because the induced voltages cancel out [36]. For a cabling scheme of the measurement system see Figure 4.3.
A shield grounding is not strictly necessary for the metallic enclosure to be an effective Faraday cage. But when grounding is done, it prevents the shield from charging up over time and of building up any potential difference between the shield and the signal leads [36] [37]. Without grounding the shield it can act as an antenna and pick up noise from time-dependent fields. For the comparison between unshielded and shielded signal leads see Figure 4.4. To distinguish between noise and real signal, the geophone was exchanged with a resistor of similar resistance (4.4A). The geophone has a series resistance of 631Ω and the test resistor 1000Ω. The expected spectrum is then a constant line because its resistance is frequency independent. The shielding effect of the grounded cable shield can be observed in the spectrum. For similar measurements

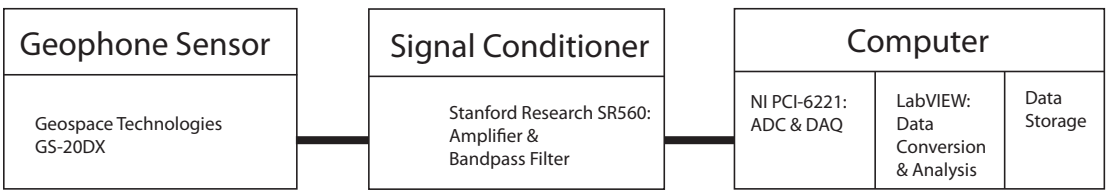

Figure 4.2: Overview about the signal path.

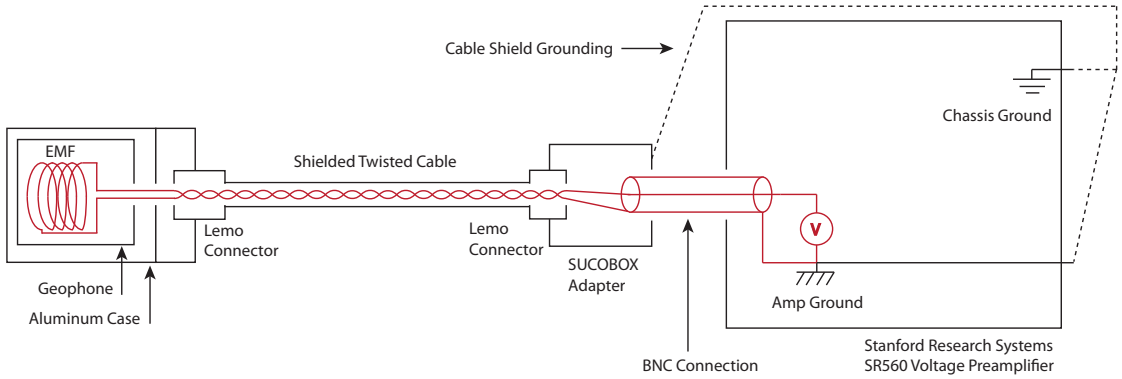

Figure 4.3: Geophone cabling scheme. Red lines represent signal leads. Black lines indicate metallic surrounding. Dashed lines are the connections for grounding the shield.

with the geophone, see Figure (4.4B). The geophone is placed on an optical table to reduce the induced signal. The reduction of the 50Hz peak as well as for frequencies $\gtrsim$350Hz is clearly visible. Note also the similar signal levels for the high frequencies of the spectrum measured with the geophone with that of the resistor. There the geophone signal is very low, probably it only acts as a resistor in this regime. Comparison between both shielded spectra (red in A and B) show that the geophone signal is well above the noise level, even on the optical table.

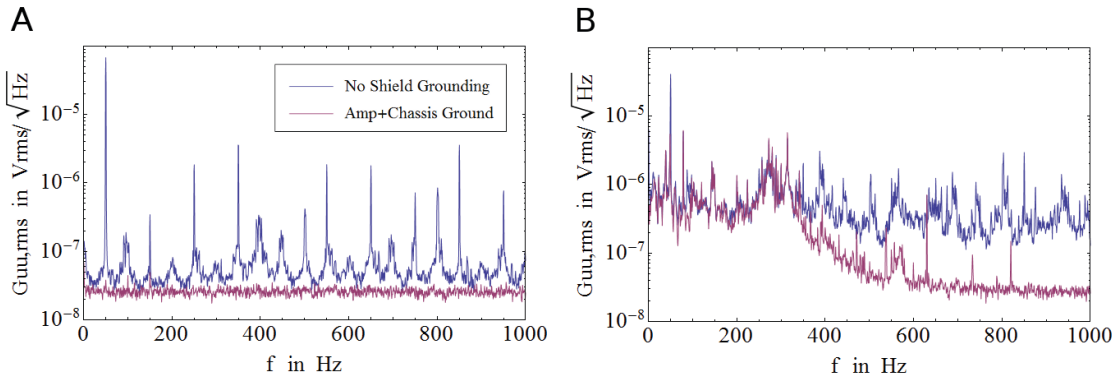

Figure 4.4: Power spectral density for cable shield grounding. A: Measurements with the geophone being exchanged with a 1000Ω resistor. B: Measurement with the geophone on an optical table.

4.2.3 Vibration Sensor - Geophone

The following description of the geophone vibration sensor are based upon references [38] and [39].

The geophone sensor *GS-20DX* from *Geospace Technologies* consists of a coil on a spring in a static magnetic field provided by a fixed magnet. The relative motion induces a voltage in the coil proportional to rate of change of magnetic flux. For horizontal and vertical measurements different versions of the sensor must be used. For an overview about the sensor see Figure 4.5.

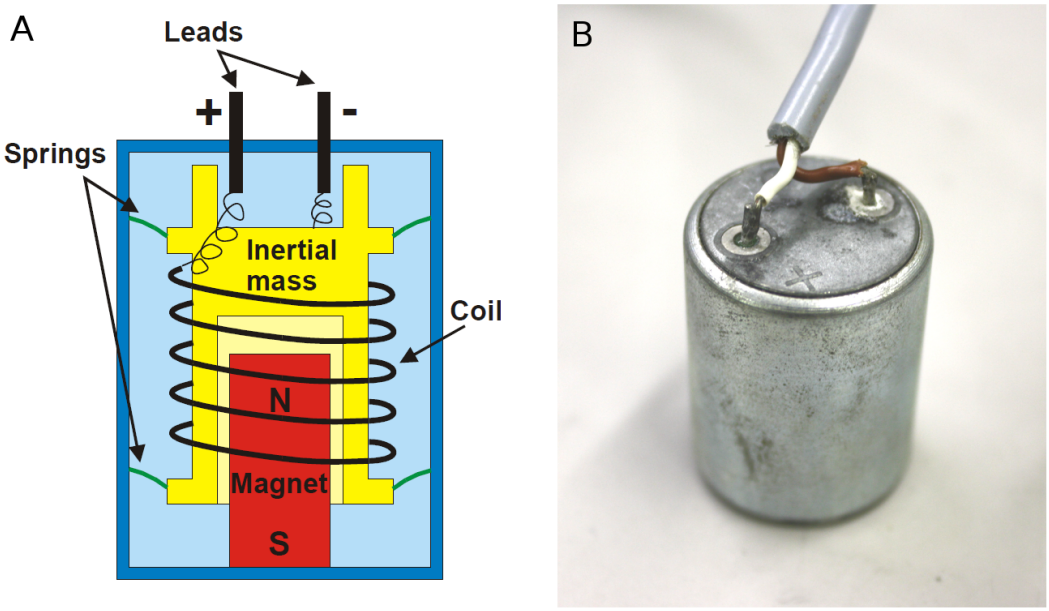

Figure 4.5: A: Geophone sketch, taken from [38]. B: Photograph of the used Geospace GS-20DX.

Figure 4.5 shows the inertial mass and the coil connected via the springs to the case. They move in the (ideally) magnetic dipole field of the permanent magnet when the case is subject to vibrations. Then a voltage

$$V_{ind} = -N\frac{d\Phi}{dt} = -N\frac{d\Phi}{dx}\dot{x} \tag{4.1}$$

is induced in the coil. N is the number of loops of the coil and Φ the magnetic flux. The variable x denotes the displacement of the mass and the coil relative to the case and the magnet. With the definition of the geophone sensitivity G

$$V_{ind} := G\dot{x} \tag{4.2}$$

we find

$$G = -N\frac{d\Phi}{dx}. \tag{4.3}$$

From Equation (4.1) we see that the geophone is intrinsically a velocity sensor since the voltage signal is proportional to velocity.

A general configuration for the operation of the geophone is when the excited geophone drives an external damping resistance R_d. Partially geophones are already equipped with such a resistance which cannot be removed. Then additional to the mechanical damping with constant D electromagnetic damping occurs and a current I will flow through the circuit. The additional damping with R_d reduces the geophone sensitivity but also reduces the overshoot at the resonance frequency, see Figure 4.7. The sensor reacts then more uniformly to vibrations. The circuit contains only the geophone and its leads are connected via the external resistor,

shown in Figure 4.6.

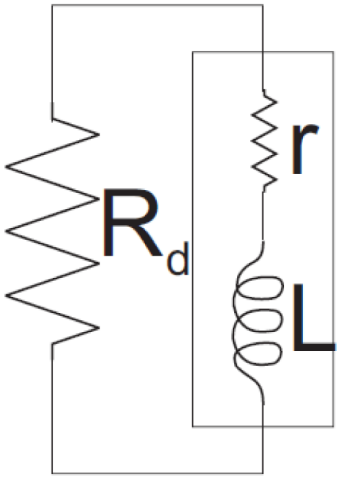

Figure 4.6: Geophone circuit with damping resistor R_d. The box on the right is a lumped element model of the geophone. Figure taken from [38].

For this circuit, Kirchhoff's mesh rule gives:

$$V_{ind} = G\dot{x} = I(R_d + r) - L\dot{I} \tag{4.4}$$

with the coil inductance L and the coil resistance r. At an excitation with frequency ω, on average $\dot{I} \approx \omega I$ and the inductive part in Equation (4.4) is negligible if $\omega L \ll R_d + r$. This inequality is usually fulfilled, but if not R_d must be increased. Hence we use

$$I = \frac{G}{R_d + r}\dot{x}. \tag{4.5}$$

The coil then acts as a magnetic dipole with magnetic dipole moment m_d=INA and effective area NA. N is the number of loops of the coil and A is the area of a single loop. The extra force on the coil resulting from the magnetic field gradient of the permanent magnet is given by

$$F = m_d \nabla B = INA\frac{dB}{dx} = IN\frac{d\Phi}{dx} = -GI = -\frac{G^2}{R_d + r}\dot{x}. \tag{4.6}$$

The force F opposes the motion of the coil and therefore damps it. The total damping constant d can be written as

$$d = D + \frac{G^2}{R_d + r}, \tag{4.7}$$

where D is the mechanical damping of the coil motion without using a damping resistor ($R_d \to \infty$). Including all sources of damping the equation of motion for the geophone is then

$$m(\ddot{x} + \ddot{q}) + d\dot{x} + kx = 0 \tag{4.8}$$

with $\ddot{q}$ the acceleration of the geophone case, $\ddot{x}$ the acceleration of the coil relative to the case and k the spring constant. Reformulating this equation with $\omega_0 = \sqrt{k/m}$ and writing the

damping as a fraction of critical damping $\alpha = \frac{d}{2m\omega_0} = \alpha_0 + \frac{G^2}{2m\omega_0(R_d+r)}$ gives

$$\ddot{x} + 2\alpha\omega_0\dot{x} + \omega_0^2 x = -\ddot{q} := a_g e^{i\omega t}, \tag{4.9}$$

where the acceleration of the case has been set to the complex number on the r.h.s.

When we set the displacement of the coil relative to the case to $x = x_c e^{i\omega t}$ and solve for x_c:

$$x_c = \frac{a_g}{(\omega_0^2 - \omega^2) + 2i\alpha\omega_0\omega}. \tag{4.10}$$

We are primarily interested in the amplitude of the signal, so we take $|v_c| = |\omega x_c|$ and $|a_g| = |\omega v_g|$. Then we can write for the induced voltage

$$|V_{ind}| = |Gv_c| = \left|\frac{G\omega^2 v_g}{(\omega_0^2 - \omega^2) + 2i\alpha\omega_0\omega}\right| = \frac{G\left(\frac{\omega^2}{\omega_0^2}\right)v_g}{\sqrt{\left(1 - \frac{\omega^2}{\omega_0^2}\right)^2 + 4\alpha^2\left(\frac{\omega^2}{\omega_0^2}\right)}}. \tag{4.11}$$

This is the total induced voltage between the leads of the coil and differs from the measured voltage for finite R_d. Assuming an infinite input resistance of the voltage amplifier when measuring the signal then a current flows only in the loop of r and R_d. The total induced voltage is then split between the resistors such that we only measure the part $V_{meas} = V_{ind}\frac{R_d}{R_d+r}$, see Figure 4.8 (there, set V_0=0 and V_1=V_{meas}). Therefore we obtain for the desired vibration in terms of velocity amplitude

$$v_g(\omega) = V_{meas}(\omega)\left(\frac{G\left(\frac{\omega^2}{\omega_0^2}\right)\left(\frac{R_d}{R_d+r}\right)}{\sqrt{\left(1 - \frac{\omega^2}{\omega_0^2}\right)^2 + 4\alpha^2\left(\frac{\omega^2}{\omega_0^2}\right)}}\right)^{-1}. \tag{4.12}$$

The angular frequency dependence has been included here for clarity.

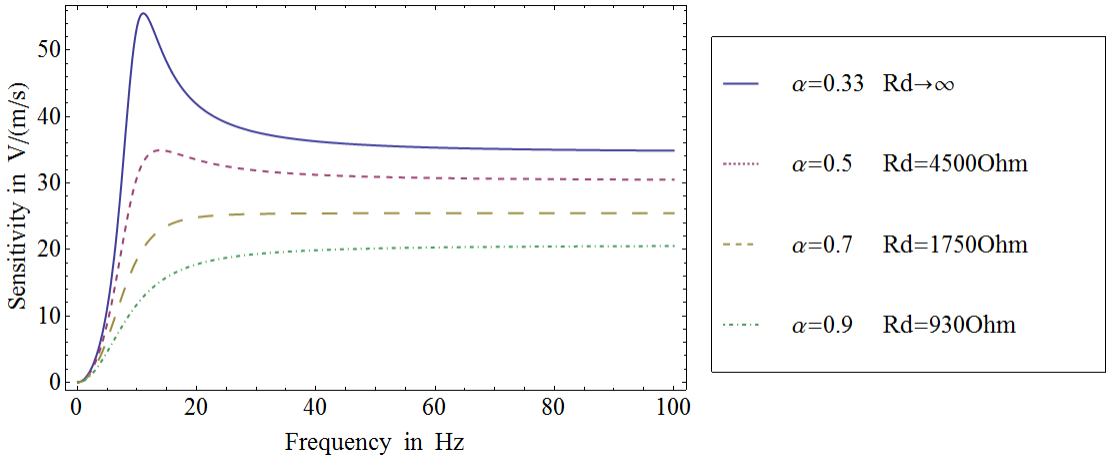

Figure 4.7: Geophone sensitivity for four different damping resistances R_d and resulting damping constants α.

The GS-20DX sensor has no implemented R_d and none is used for the measurements such that the last modification $\frac{R_d}{R_d+r} = 1$ because $R_d \to \infty$. The relevant parameters for the

last equation (G, f_0, α) can be determined with a calibration and (r, R_d) directly measured. The only parameter that has to determined by the manufacturer is the mass of the "moving mass" which is necessary for fitting α from the calibration measurements. The automated calibration method from Emile Hoskinson is a big help for determining G, f_0 and α and will be explained below.

4.3 Calibration

In this part the calibration procedure for the geophone sensor is described. This includes the description of the software to measure geophone specific parameters and the underlying theory.

4.3.1 Calibration Of The Sensors

For the conversion between velocity and voltage several parameters are needed, see Equation (4.12). To determine the geophone parameters precisely a LabVIEW program is used, written by Emile Hoskinson. The circuit used with the program is shown in Figure 4.8 and includes the additional damping resistance R_d for full generality. The analysis below is based on reference [38].

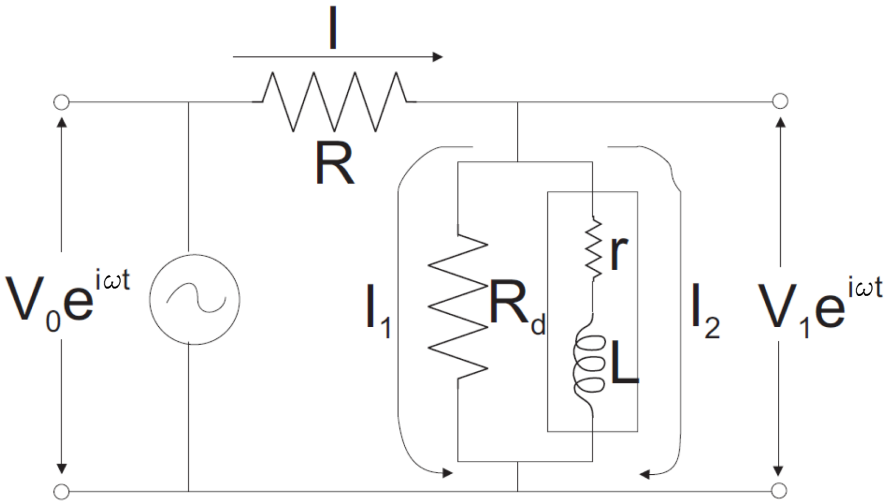

Figure 4.8: Circuit for automated calibration. Figure taken from [38].

The idea behind the method is to place a series resistor R in the circuit, apply a sine wave voltage $V_0 e^{i\omega t}$ to excite the geophone at a single frequency, measure the response $V_1 e^{i\omega t}$ and sweep the frequency of the excitation ω. From the response the parameters can then be fitted.

Using Kirchhoff's mesh rule in the circuit from Figure 4.8 we find

$$V_0 e^{i\omega t} + G\dot{x} = IR + I_2 r, \tag{4.13}$$

where the sources of the emf are on the l.h.s. and the resulting voltage drops are on the r.h.s. We neglect the inductive part of the coil as before. Furthermore,

$$V_1 e^{i\omega t} = V_0 e^{i\omega t} - IR = I_2 r - G\dot{x}. \tag{4.14}$$

The calibration parameters are obtained from a fit to the function $\frac{V_1}{V_0}$.
To eliminate the current I we note that:

$$I = I_1 + I_2, \tag{4.15}$$

$$I_1 R_d = I_2 r, \tag{4.16}$$

$$I = I_2 \left(1 + \frac{r}{R_d}.\right) \tag{4.17}$$

From the balance of forces on the coil, including the electromagnetic damping term GI_2 (like in Equation (4.6)),

$$m\ddot{x} = -GI_2 - D\dot{x} - kx. \tag{4.18}$$

We can find I_2 by rewriting the equation to

$$\ddot{x} + 2\alpha_0\omega_0\dot{x} + \frac{G}{m}I_2 + \omega_0^2 x = 0 \tag{4.19}$$

with $\omega_0 = \sqrt{\frac{k}{m}}$ and $\alpha_0 = \frac{D}{2m\omega_0}$. Plugging in $\dot{x} = v_0 e^{i\omega t}$ with v_0 maybe complex we then find

$$I_2 = -\left(D + im\omega\left(1 - \frac{\omega_0^2}{\omega^2}\right)\right)\frac{v_0 e^{i\omega t}}{G}. \tag{4.20}$$

Now we can use Equations (4.17) and (4.20) in Equations (4.13) and (4.14) to calculate the fraction

$$\frac{V_1}{V_0} = \frac{I_2 r - G\dot{x}}{IR + I_2 r - G\dot{x}} = c + \frac{2sc(1-c)}{2\alpha_0 + 2sc + iz} \tag{4.21}$$

with constants

$$c = \frac{rR_d}{rR_d + RR_d + rR}, \qquad s = \frac{G^2}{2m\omega_0 r}, \qquad z = \frac{\omega}{\omega_0}\left(1 - \frac{\omega_0^2}{\omega^2}\right). \tag{4.22}$$

For $R_d \to \infty$, $c = \frac{r}{r+R}$. This yields the magnitude and phase of the ratio

$$\left|\frac{V_1}{V_0}\right| = c\sqrt{1 + \frac{4b(2\alpha_1 + b)}{4\alpha_1^2 + z^2}} \tag{4.23}$$

and

$$\theta = \arctan\left(\frac{Im(V_1/V_0)}{Re(V_1/V_0)}\right) = \arctan\left(\frac{-z}{2\alpha_1 + \frac{1}{2b}(4\alpha_1^2 + z^2)}\right) \tag{4.24}$$

with constants

$$\alpha_1 = \alpha_0 + sc, \qquad b = s(1-c). \tag{4.25}$$

Measuring the magnitude and the phase of $\frac{V_1}{V_0}$ provides two independent ways of determining the parameters of the geophone. Fitting to Equations (4.23) and (4.24) with parameters α_1, b and ω_0 provides the constants G, α_0 and f_0.

The program

At the moment the calibration software has implemented the version with $R_d \to \infty$ but in case a geophone is used with finite R_d the effort to adapt the formulas should be low. A screenshot of the software is shown in Figure 4.9.

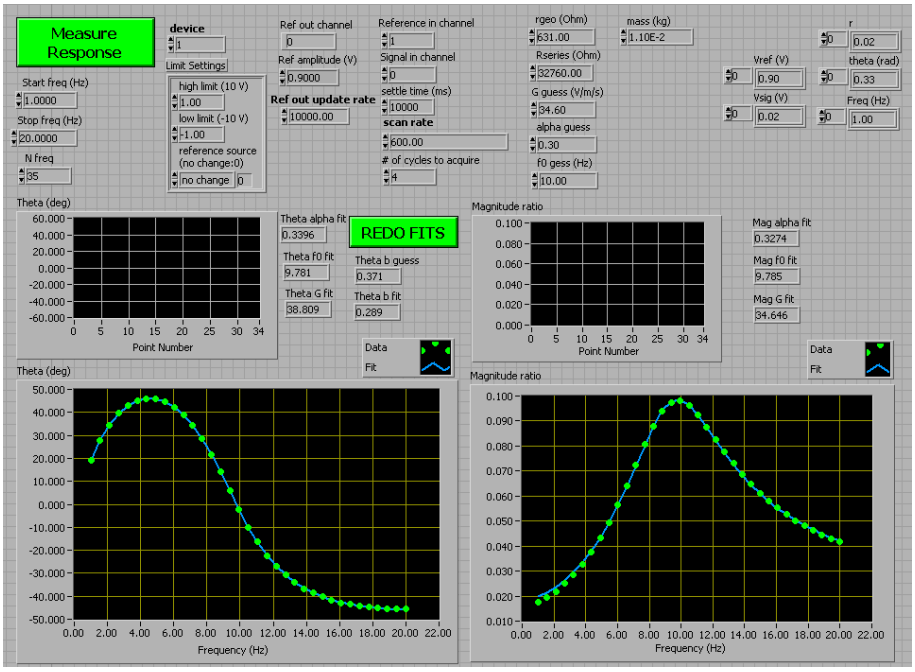

Figure 4.9: Calibration program from Emile Hoskinson. The lower left graph shows the phase response θ of the fraction $\frac{V_1}{V_0}$ and the lower right shows the magnitude ratio. Green dots are measured data, blue line is the fit.

Measured geophone parameters for all three sensors are shown in Table 4.1.

Geophone	α	G in V/(m/s)	f_0 in Hz
Vertical	0.33	34.6	9.78
Horizontal 1	0.33	33.8	9.91
Horizontal 2	0.31	32.9	10.15
Manufacturer	0.3±10%	34.6	10

Table 4.1: Calibration parameters for the different geophones.

The measured values are quite close to the standard values provided by the manufacturer. Additional geophone parameters are the series resistance r=631Ω and the mass m=11g.

4.4 Theory

This section explains how the vibration spectrum is calculated and its conversion between different units.

4.4.1 The Power Spectral Density

To analyze the vibration data of stationary random vibrations the Power Spectral Density (PSD) of the signal is calculated.
Assume we measure a signal U(t) from the geophone then we are in general mostly interested in its frequency components. Therefore, we compute the one-sided PSD $G_{UU}(f)$ [34, p. 19.8] as

$$G_{UU}(f) = \lim_{T\to\infty} \frac{2}{T} \left\langle |U(f,T)|^2 \right\rangle \qquad f > 0 \tag{4.26}$$

with the Fourier transform

$$U(f,T) = \int_0^T U(t) e^{-2\pi i f t} dt. \tag{4.27}$$

The factor of 2 in Equation (4.26) comes from the $f > 0$ condition. The term "power" occurs because the spectrum is calculated with the square of the signal. Since the spectrum cannot be measured infinitely long ($T \to \infty$) there will be a potential random error associated with that. The brackets $\langle ... \rangle$ denote the expectation value and imply an ensemble average. The root mean square spectrum is obtained by taking the square root:

$$G_{UU,rms}(f) = \sqrt{G_{UU}(f)} = \sqrt{\lim_{T\to\infty} \frac{2}{T} \langle |U(f,T)|^2 \rangle}. \tag{4.28}$$

The unit of $G_{UU}(f)$ is V^2/Hz and consequently for $G_{UU,rms}(f)$ $V_{rms}/\sqrt{Hz}$.
The average power in a given frequency band from f_1 to f_2 $P_{UU}(f_1,f_2)$ is evaluated by the corresponding integral over $G_{UU}(f)$,

$$P_{UU}(f_1, f_2) = \int_{f_1}^{f_2} G_{UU}(f) df. \tag{4.29}$$

T is the measurement time T_{meas} and determines the lowest frequency as well as the bin width $\Delta f = \frac{1}{T_{meas}}$. The data acquisition system takes the power in a specific frequency bin and divides it by the bin width Δf [40] to calculate the power spectral density.
The reason of dividing the spectrum by the bandwidth is to make sense of wideband noise [40]. For instance assume a white noise signal that is characterized by having the signal power uniformly distributed in frequency space. The amplitude (power) in a specific frequency bin depends in general on the bin width because taking more spectral components into one bin increases the power per bin. Therefore the amplitude would depend on the resolution of the spectrum. In the ideal case of a white noise spectrum the division by the bin width provides a constant value and the informative value of the spectrum is higher than without this division. Therefore, the PSD contains a division by the bandwidth.

4.4.2 Conversion Of Power Spectral Densities

Since we are interested in mechanical quantities like acceleration, velocity and displacement we must convert our obtained voltage amplitude $V_{meas}(f)$=U(f,T). The conversion from $V_{meas}(f)$ to geophone case (or ground) velocity amplitude $v_g(f)$ is given by Equation (4.12)

with $\omega = 2\pi f$. Velocity information might not be the most interesting quantity in any case. Therefore we must convert the quantities and spectra [41].

Now assume $v_g(f)$ and $\tilde{v}_g(t)$ are connected by Fourier transform and are complex in general, then

$$\tilde{v}_g(t) = \int_{-\infty}^{\infty} v_g(f) e^{2\pi i f t} df, \tag{4.30}$$

and similar for the displacement $\tilde{x}_g(t)$ and the acceleration $\tilde{a}_g(t)$. We know that

$$\tilde{a}_g(t) = \frac{d\tilde{v}_g(t)}{dt} = \frac{d^2\tilde{x}_g(t)}{dt^2}. \tag{4.31}$$

Combining Equation (4.31) with (4.30) we find that

$$\tilde{a}_g(t) = \frac{d}{dt}\int_{-\infty}^{\infty} v_g(f) e^{2\pi i f t} df = \int_{-\infty}^{\infty} [2\pi i f v_g(f)] e^{2\pi i f t} df. \tag{4.32}$$

Comparing with the definition

$$\tilde{a}_g(t) = \int_{-\infty}^{\infty} a_g(f) e^{2\pi i f t} df \tag{4.33}$$

we see that

$$a_g(f) = 2\pi i f v_g(f) = i\omega v_g(f). \tag{4.34}$$

Similarly, for $x_g(f)$

$$v_g(f) = 2\pi i f x_g(f) = i\omega x_g(f) \tag{4.35}$$

is obtained. This enables the conversion between the (complex) quantities via the relation

$$a_g(f) = i\omega v_g(f) = -\omega^2 x_g(f). \tag{4.36}$$

Since we are not interested in the phase of the vibrations we can convert our real amplitudes from the spectrum with

$$|a_g(f)| = \omega |v_g(f)| = \omega^2 |x_g(f)|. \tag{4.37}$$

Finally, since the power spectral density is quadratic in the signal we convert between spectra with

$$G_{aa}(f) = \omega^2 G_{vv}(f) = \omega^4 G_{xx}(f) \tag{4.38}$$

For the rms-spectra obviously

$$G_{aa,rms}(f) = \omega G_{vv,rms}(f) = \omega^2 G_{xx,rms}(f). \tag{4.39}$$

4.5 Measurements And Results

4.5.1 Consistency Check Measurement

To see whether the geophone works properly a consistency check is very helpful. For instance a known quantity can be measured with the developed methods and compared to the quantity. The method used here is to subject the geophone to a known oscillation with defined displacement. This is done with fixing the geophone to a CNC-machine which repeatedly moves the sensor up and down. The amplitude of the oscillation was set to 50μm. Then a vibration spectrum was taken. In addition, a spectrum was taken without the machine moving up and down for comparison, see Figure 4.10. The graph A shows the resulting velocity vibration spectra. One can see the many harmonics of the fundamental frequency of 0.72Hz when the machine was turned on. In comparison with the measurement where the machine was turned off the many peaks are missing. Therefore they correspond to the motion of the sensor.

Number of measurement points	2^19
Sampling rate	10KHz
Measurement time	52.4s
Frequency range	0.019-5000Hz
Averages	1
Bandpass	0.03-1000Hz
Gain	50

Table 4.2: Spectral parameters for the consistency check vibration measurement with the CNC machine, Figure 4.10. The first five parameters are set in the LabVIEW program, the last two at the preamplifier.

Similar to obtaining the average power of the signal by integrating $G_{UU}(f)$ over a specific frequency range one can obtain an average acceleration, velocity and displacement. Therefore from the spectra we calculate the rms-displacement amplitude as

$$X_{int,rms}(f_1, f_2) = \sqrt{P_{xx}(f_1, f_2)} = \sqrt{\int_{f_1}^{f_2} G_{xx}(f)df}. \tag{4.40}$$

This quantity is shown in graph B. Starting frequency for integration is f_1=f and final frequency is f_2=300Hz. Integrating over the whole frequency range from f_1=0.5Hz to 300Hz such that we just include the fundamental frequency gives a value for the rms-displacement amplitude of 47.5μm. This value is comparable to the set 50μm amplitude. Therefore we can conclude that the used method is reasonable.

4.5.2 Building Vibrations In Rooms HPF B22 & HPT C4.1

Spectra At Different Locations

As has been mentioned before vibrations can have detrimental influence on the experiments. Therefore, they have to be reduced as much as possible. In order to characterize different possible locations for the setup to be positioned, vibration spectra have been taken. The

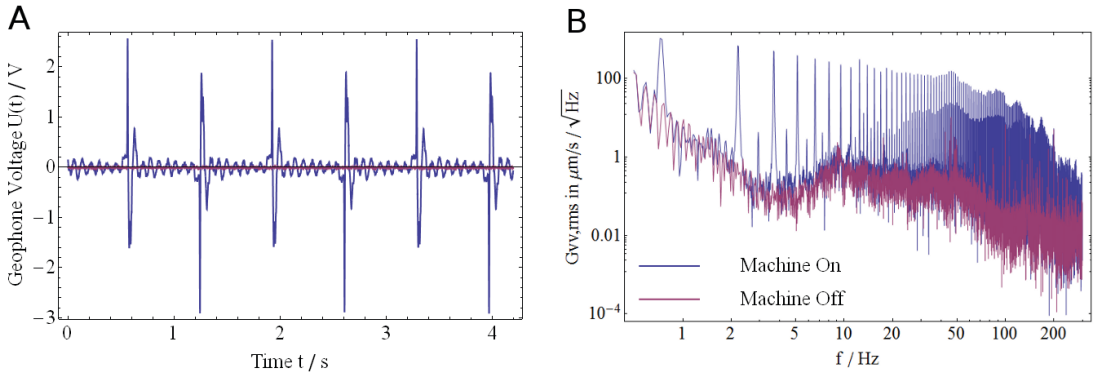

Figure 4.10: Geophone signal and vibration spectrum of a consistency check measurement done with a CNC-machine.. A: Vibration induced voltage in the geophone. B: Velocity power spectral density for this vibrations.

results for rooms HPF B22 and HPT C4.1 at ETH Hönggerberg are shown in Figure 4.11. The measurement parameters are shown in Table 4.3.

Number of measurement points	2^19
Sampling rate	10KHz
Measurement time	52.4s
Frequency range	0.019-5000Hz
Averages	10
Bandpass	0.03-1000Hz
Gain	1000

Table 4.3: Spectral parameters for the building vibration measurements, Figure 4.11. The first five parameters are set in the LabVIEW program, the last two at the preamplifier.

The spectra shown are taken on the floor of the corresponding room and measured along the vertical direction. The letters B and C in the room names indicate the floor where C is the first floor and B is one below in the basement. Graph A in the figure shows velocity spectra. Clearly at almost all frequencies the vibrations are higher in the HPT C4.1 room.

Room	$X_{int,rms}$ in nm
HPF B22	107.0
HPT C4.1	139.8

Table 4.4: Measured vertical rms-displacement amplitudes in the frequency range of 0.5Hz-300Hz.

This indicates that the HPF B22 room is suited better for the experiment in terms of vibrations.

Long Term Measurements From Different Locations

The previous considerations take only one spectrum into account. This means they represent the conditions in a very short time span of typically up to a minute. Since the conditions are influencing experiments at all times the characterization should provide information about

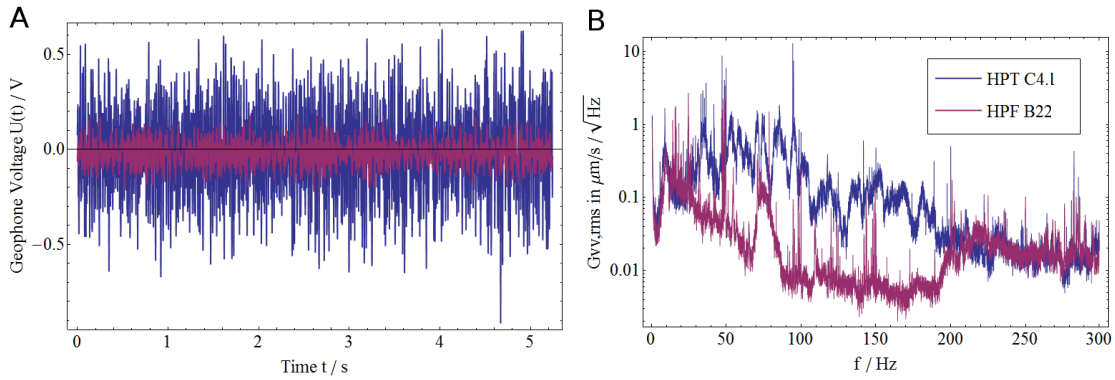

Figure 4.11: Geophone signal and spectrum of the vibration measurements taken on the floor of two rooms in different buildings. A: Vibration induced voltage in the geophone. B: Velocity power spectral density for this vibrations.

the time dependence of the vibration. In the buildings HPF & HPT from before vibration spectra have been taken repeatedly over at least one day. The rms-acceleration $A_{int,rms}$ for the vertical direction has been calculated from the spectra in three different frequency bands. Results can be seen in Figure 4.12 and Table 4.6, measurement parameters in Table 4.5.

Number of measurement points	2^14
Sampling rate	5KHz
Measurement time	3.3s
Frequency range	0.3-2500Hz
Averages	5
Bandpass	0.03-1000Hz
Gain	1000

Table 4.5: Spectral parameters for the long-term building vibration measurements, Figure 4.12. The first five parameters are set in the LabVIEW program, the last two at the preamplifier.

The principle difference between the two rooms is that B22 is a used laboratory whereas C4.1 is unused so far. Therefore human activities in the rooms are influencing the conditions only in B22.

Starting with the smallest frequency band ranging from 0.3-10Hz we compare graphs B3 and C3. In this low frequency band it is observable that in both rooms the vibrations have a large spread at times between approximately 5a.m. and 1a.m. on the next day. At night from 1a.m. until 5a.m. the vibrations are considerably smaller and are relatively constant. Since this structure appears in two different room and in two different buildings independently it is suggested that it has to do with common building services switched off at night. It is also observable that this effect happens regularly. The average vibrations are higher in room C4.1 in this frequency band.

Next the frequency band is increased to 0.3-100Hz, see graphs B2 and C2. Like before the vibrations are lowest at night in both graphs but the effect is larger in B2. Unlike before the reduction appears slowly such that an oscillatory behavior is visible in C2. Whether the

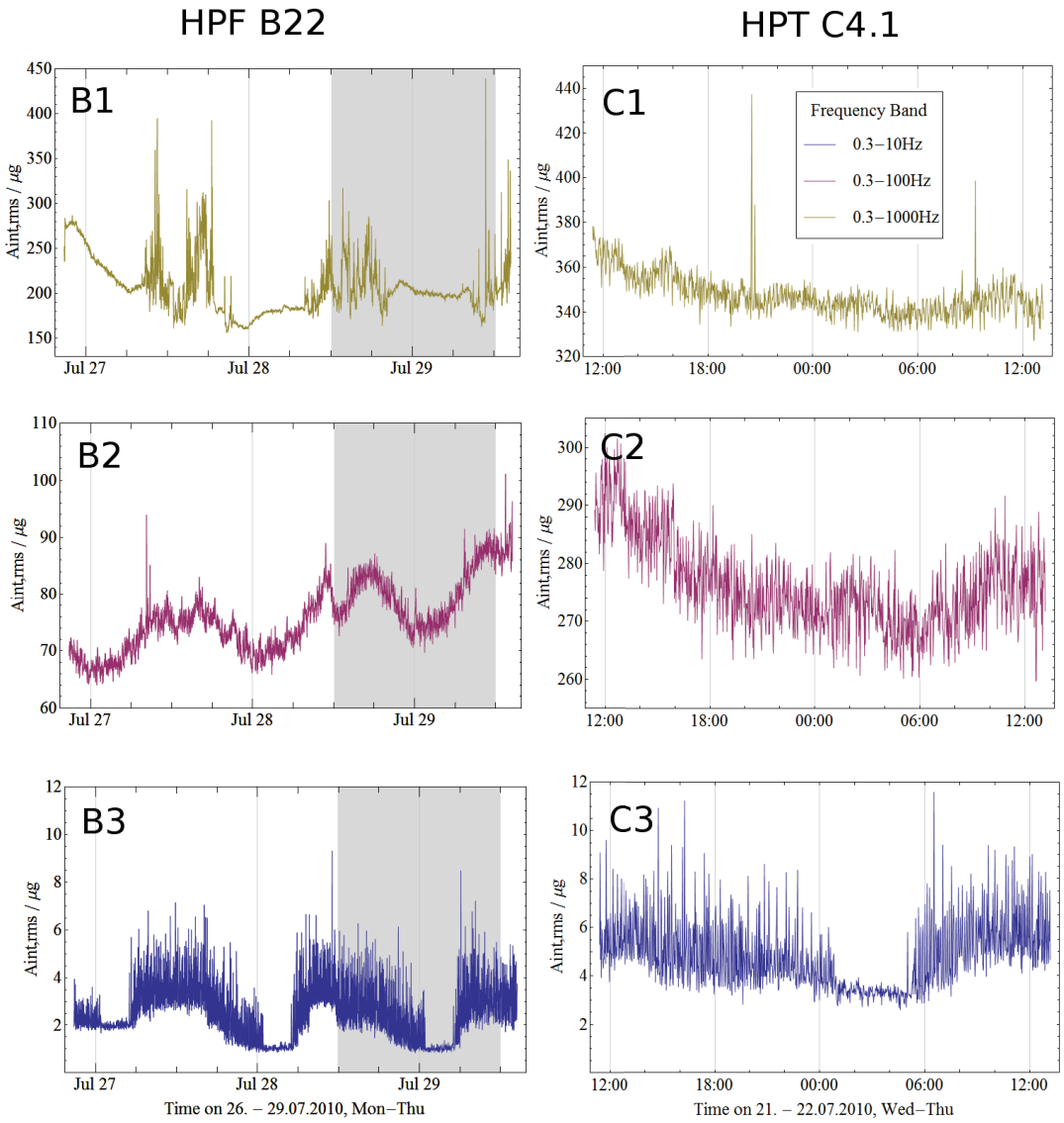

Figure 4.12: Time dependence of the band integrated rms-acceleration for two different rooms and three different frequency bands. The gray area in graphs B1-B3 indicates a time span comparable to the measurements in C1-C3.

curve oscillates in C2 is unknown. Large deviations from the average vibration background appear only very rarely in B2 and do not appear in C2. The overall vibration level is much larger in room C4.1 in this frequency range.

Finally the frequency band is further increased to 0.3-1000Hz. In graph B1 a difference between day and night is observable. The variability of the vibrations is relatively large at times when laboratory staff works. At night the vibration signal is reduced but not always constant. In graph C1 for room C4.1 night and day are hard to distinguish. The signal is almost constant, it changes only relatively little over time. Deviations from this background level do only occur near 20:30 o'clock and 9:30am. These times coincide with possible working times in laboratories. The increase of signal level compared with the frequency band before is relatively small.

Frequency Band	0.3-10Hz			0.3-100Hz			0.3-1000Hz		
Statistics	Min.	Avg.	Max.	Min.	Avg.	Max.	Min.	Avg.	Max.
HPF B22	0.84	2.54	9.31	64.0	75.9	101	156	207	439
HPT C4.1	2.60	4.81	11.6	260	276	302	327	347	437

Table 4.6: Statistical values from Figure 4.12. The unit is μg.

From this analysis it can be seen that even with laboratory staff working mainly on the other side of the room B22 the vibration level is comparable or smaller than in the empty room C4.1. This indicates again that room B22 would be suited better for the experiment.

4.5.3 Vibrations Of A Cryostat

With the same methods as in the previous Section 4.5.1 we have analyzed the vibrations of the pulse tube cooler in the vacuum chamber. Since this vibration source is in the experiment it is even more important. The setup for the measurements is shown in Figure 4.13.

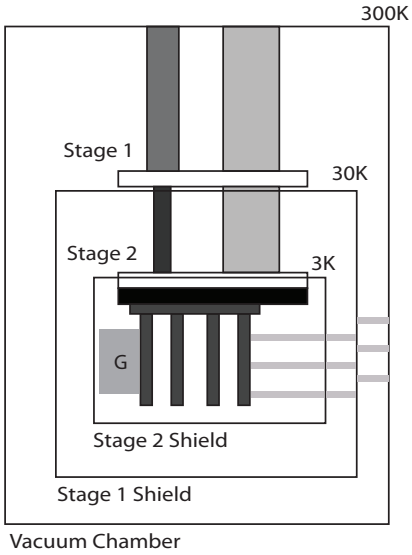

Figure 4.13: Configuration for the cryostat vibration measurements. The gray rectangle with the "G" denotes the vibration sensor.

The geophone sensor is tightly fixed with screws to the electrodes. The electrodes are connected to the shields and the vacuum chamber with plastic spacers. The measurements are in the vertical direction. Results of the measurements can be seen in Figure 4.14 and measurement parameters in Table 4.7.
From the velocity spectrum $G_{vv,rms}$ we determine the fundamental frequency of 1.41Hz for the pulse tube cooling cycle. Many harmonics are also visible. The devices that are switched on for the operation of the whole cryostat are the two vacuum pumps and the pulse tube cooler. The signal level is significantly lower when these devices are not in use. For the displacement the parameter $X_{int,rms}$ is calculated. The frequency range for integration is from f_1=0.5Hz to f_2=300Hz as before and includes also the fundamental frequency of the pulse tube cycle. The rms-displacement amplitude in this frequency band is then determined as 13.9μm.

Number of measurement points	2^19
Sampling rate	10KHz
Measurement time	52.4s
Frequency range	0.019-5000Hz
Averages	1
Bandpass	0.03-1000Hz
Gain	100

Table 4.7: Spectral parameters for the pulse tube vibration measurement, Figure 4.14. The first five parameters are set in the LabVIEW program, the last two at the preamplifier.

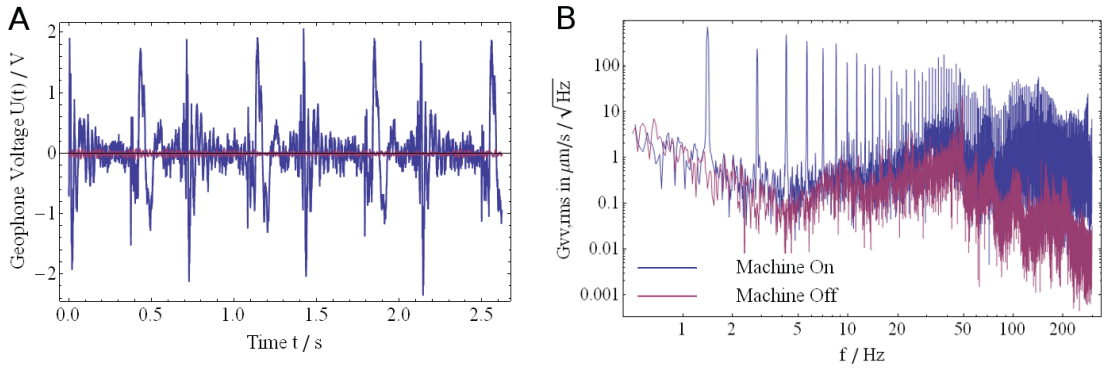

Figure 4.14: Geophone signal and vibration spectrum of pulse tube cooler stage 2 in vertical direction. A: Vibration induced voltage in the geophone. B: Velocity spectrum.

Fortunately, after the measurements with the geophone I received data on this issue from the manufacturer Cryomech Inc. for the same pulse tube cooler, see Figure 4.15.
The overall drift of the displacement shows that the length of the pulse tube changes when it cools down. On top of the drift is the oscillatory behavior caused by the pressure changes in the pulse tube cooler when in operation. The inset shows a zoomed version of the graph. From the inset we see that the oscillation has an amplitude of about 10μm. This value is comparable to the rms-displacement amplitude of 13.9μm determined with the geophone and provided another consistency check.

4.6 Conclusions

The first thing that we can conclude from the previous measurements and results is that the construction of a vibration measurement system was successful and the method for measuring vibrations works reasonably well. Therefore the theoretical model of the geophone seems to include the important properties of the geophone.

Second, from the vibration measurements in rooms HPF B22 and HPT C4.1 the determined rms displacement amplitude of 107.0nm (B22) is lower than 139.8nm (C4.1) and therefore shows that room B22 is suited better for experiments where vibrations influence the measurement results.

Third, from the repeated measurements over at least one day we conclude that laboratory

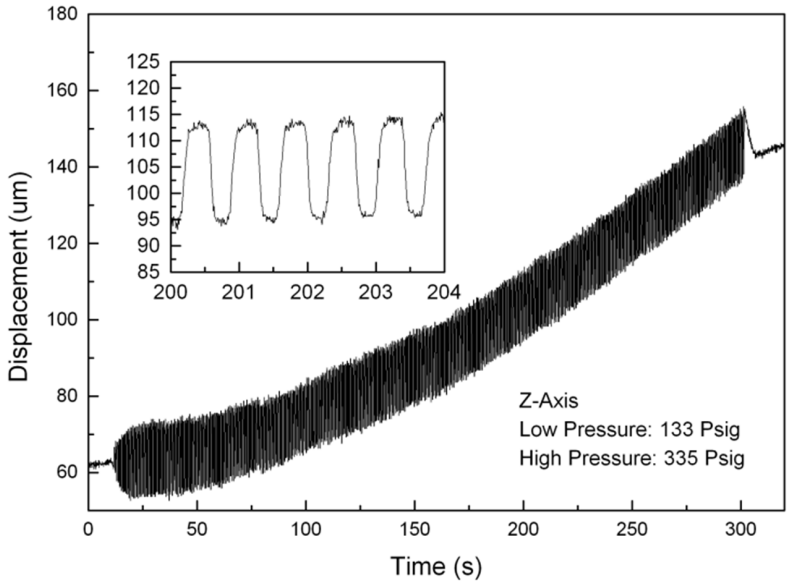

Figure 4.15: Measurements from the manufacturer Cryomech. The graph shows the vertical displacement of stage 2 of the pulse tube under operation.

staff activity in the room has a significant influence on the acceleration vibration spectrum but mostly for frequencies in the range of 100Hz or larger.

Fourth, the parking garage close to the HPT building does not lead to a dramatic increase of vibrations over the average level because the acceleration amplitude is relatively constant over time. There are only three events monitored that would be interpreted as significantly larger than average but they cover only a time span of several minutes. If cars entering and leaving the parking garage would have a measurable influence on the spectra, this should be seen over a time span of hours, preferably in the morning and in the evening.

Fifth, the investigation of vibration measurements for the pulse tube cooler showed that this source of vibrations dominates clearly over the building vibrations. The determination of the rms displacement amplitude of 13.9μm of the second stage of the pulse tube in vertical direction was supported by measurements of the manufacturer Cryomech.

4.7 Summary

In the preceding chapter a vibration measurement system was explained and used for measurements.

First, in an introductory part the nature of vibrations was presented. This includes the properties of vibrations like deterministic, random, stationary and non-stationary types. Also sources of vibrations were mentioned and that vibrations can influence the precision of control and the measurements of the atoms.

Second, the measurement setup was explained. It consists of the vibration sensor which is connected to a preamplifier and further to the PC via an analog-to-digital converter card.

The vibration sensor is in principle a coil on a spring in a static magnetic field. The induced signal of the coil in the magnetic field, V_{ind}, is proportional to the velocity of the coil relative to the magnet v_c. A theoretical model of the sensor was developed to convert the voltage from the sensor to the velocity of the sensor case and therefore the velocity of the object where the sensor is mounted. To obtain this velocity v_g from the measured voltage V_{meas} one has to take into account the suspension of the coil via springs (with angular resonance frequency ω_0) and potentially additional damping with an external resistor R_d. For frequencies $\omega \ll \omega_0$ the sensitivity reduces significantly compared to the intrinsic sensitivity G, for $\omega \approx \omega_0$ the sensitivity is larger than G and for $\omega \gg \omega_0$ it approaches G.

Third, the calibration method was explained theoretically. The circuit was slightly changed to excite the sensor with a known voltage signal V_0 and measure its response V_1. From the ratio V_1/V_0 sensor parameters of three geophones were fitted. The parameters are the resonance frequency of the sensor f_0, its intrinsic sensitivity G and its damping in terms of critical damping α.
Furthermore it was explained how to obtain the power spectral density $G_{UU}(f)$ of the vibration signal $U(t)$ and that the conversion between acceleration ($G_{aa}(f)$), velocity ($G_{vv}(f)$) and displacement ($G_{xx}(f)$) types is done with a simple multiplication/division by ω^2 and ω^4 respectively.
Also the power in a specific frequency range $P_{UU}(f_1, f_2)$ was calculated as the integral of the power spectral density to mainly obtain mechanical vibration quantities like rms-acceleration, -velocity and -displacement.

Fourth, the method of obtaining vibration spectra and extracting mechanical quantities like rms-displacement amplitude was tested by mounting the sensor to a CNC-machine which displaces the sensor with a known amplitude. This measurement showed that with integrating the displacement spectrum $G_{xx}(f)$ from 0.5Hz-300Hz the obtained rms-displacement amplitude of 47.5μm comes close to the set 50μm amplitude. This verified that the used methods for obtaining a displacement amplitude are reasonable.
The sensor was used to measure the vibrations of two rooms. The rms-displacement amplitude was determined at the floor of both rooms in vertical direction at one time. It showed that room HPF B22 (107.0nm) is suited better for experiments than room HPT C4.1 (139.8nm) using the frequency range of 0.5Hz-300Hz. Additionally the rms-acceleration amplitude was monitored over at least one day repeatedly. It turned out that a reduction of vibrations is observable over night and that one can clearly identify vibrations from humans and machines when including frequencies up to 1000Hz in the analysis.
The pulse tube cooler for cooling the experiments was tested with the same methods as before, too. The rms-displacement amplitude of the second stage in the vertical direction was determined as 13.9μm. Measurements from the manufacturer support this value. The leading source of vibrations is the pulse tube cooler.

Acknowledgment

At first I would like to thank Professor Dr. Andreas Wallraff for giving me the opportunity to carry out my master thesis in his research group. His explanations and ideas were always very helpful.

Special thanks go to my supervisor Dr. Stefan Filipp for helping me how to deal with problems that arose in the course of the thesis and because of the proofreading of the thesis.

I greatly enjoyed the discussions, the work and the table tennis games with Christian Gross, too.

The help from Christian Lang, Romeo Bianchetti and Johannes Fink as well as from the rest of the Qudev group was excellent.

I also want to thank the members from the collaborating group of Professor Merkt. Especially to mention for their kind support are Professor Dr. Frédéric Merkt, Dr. Stephen Hogen, Dr. Urs Hollenstein, Joseph Agner and Hansjürg Schmutz.

Thank goes also to Chao Wang from Cryomech for providing further vibration data from the pulse tube cooler.

And finally I want to thank my parents Uta and Uwe for their invaluable and continuous support during my whole physics studies.

Bibliography

[1] Michael A. Nielsen and Isaac L. Chuang. *Quantum Computation and Quantum Information*. Cambridge University Press, 2007.

[2] Lieven M. K. Vandersypen, Matthias Steffen, Gregory Breyta, Costantino S. Yannoni, Mark H. Sherwood, and Isaac L. Chuang. Experimental realization of Shor's quantum factoring algorithm using nuclear magnetic resonance. *Nature*, 414:883–887, 2001.

[3] Stephan Gulde, Mark Riebe, Gavin P. T. Lancaster, Christoph Becher, Jürgen Eschner, Hartmut Häffner, Ferdinand Schmidt-Kaler, Isaac L. Chuang, and Rainer Blatt. Implementation of the Deutsch-Jozsa algorithm on an ion-trap quantum computer. *Nature*, 421:48–50, 2003.

[4] S. J. van Enk, H. J. Kimble, and H. Mabuchi. Quantum information processing in cavity-qed. *Quantum Information Processing*, 3(1-5):75–90, 2004.

[5] Serge Haroch and Jean-Michel Raimond. *Exploring the Quantum*. Oxford Graduate Texts, 2007.

[6] Andreas Wallraff. Quantenmechanik mit Schaltkreisen. *Physik Journal*, 12:39–45, 2008.

[7] Alexandre Blais, Ren-Shou Huang, Andreas Wallraff, S. M. Girvin, and R. J. Schoelkopf. Cavity quantum electrodynamics for superconducting electrical circuits: An architecture for quantum computation. *Physical Review A*, 69(6):062320, Jun 2004.

[8] Andreas Fragner. Coupling superconducting qubits to tunable cavities and resolving the lamb shift in circuit qed. Diploma thesis, Vienna University of Technology, 2008.

[9] David Isaac Schuster. *Circuit Quantum Electrodynamics*. PhD thesis, Yale University, 2007.

[10] Yuriy Makhlin, Gerd Schön, and Alexander Shnirman. Quantum-state engineering with josephson-junction devices. *Reviews of Modern Physics*, 73(2):357–400, May 2001.

[11] I. Chiorescu, P. Bertet, K. Semba, Y. Nakamura, C. J. P. M. Harmans, and J. E. Mooij. Coherent dynamics of a flux qubit coupled to a harmonic oscillator. *Nature*, 431:159–162, 2004.

[12] A. Fragner, M. Göppl, J. M. Fink, M. Baur, R. Bianchetti, P. J. Leek, A. Blais, and A. Wallraff. Resolving vacuum fluctuations in an electrical circuit by measuring the lamb shift. *Science*, 322:1357–1360, 2008.

[13] Thomas F. Gallagher. *Rydberg Atoms*. Cambridge University Press, 1994.

[14] J. A. Schreier, A. A. Houck, Jens Koch, D. I. Schuster, B. R. Johnson, J. M. Chow, J. M. Gambetta, J. Majer, L. Frunzio, M. H. Devoret, S. M. Girvin, and R. J. Schoelkopf. Suppressing charge noise decoherence in superconducting charge qubits. *Physical Review B*, 77(18):180502, May 2008.

[15] Thomas F. Gallagher. Rydberg atoms. *Reports on Progress in Physics*, 51:143–188, 1988.

[16] Myron L. Zimmerman, Michael G. Littman, Michael M. Kash, and Daniel Kleppner. Stark structure of the rydberg states of alkali-metal atoms. *Physical Review A*, 20(6):2251–2275, Dec 1979.

[17] J. A. Jones and M. Mosca. Implementation of a quantum algorithm on a nuclear magnetic resonance quantum computer. *Journal of Chemical Physics*, 109:1648–1653, 1998.

[18] P. Domokos, J. M. Raimond, M. Brune, and S. Haroche. Simple cavity-qed two-bit universal quantum logic gate: The principle and expected performances. *Physical Review A*, 52(5):3554–3559, Nov 1995.

[19] Xiaoqin Li, Yanwen Wu, Duncan Steel, D. Gammon, T. H. Stievater, D. S. Katzer, D. Park, C. Piermarocchi, and L. J. Sham. An all-optical quantum gate in a semiconductor quantum dot. *Science*, 301:809–811, 2003.

[20] J. Majer, J. M. Chow, J. M. Gambetta, Jens Koch, B. R. Johnson, J. A. Schreier, L. Frunzio, D. I. Schuster, A. A. Houck, A. Wallraff, A. Blais, M. H. Devoret, S. M. Girvin, and R. J. Schoelkopf. Coupling superconducting qubits via a cavity bus. *Nature*, 449:443–447, 2007.

[21] R. J. Schoelkopf and & S. M. Girvin. Wiring up quantum systems. *Nature (London, United Kingdom)*, 451:664–669, 2008.

[22] Anders S. Sørensen, Caspar H. van der Wal, Lilian I. Childress, and Mikhail D. Lukin. Capacitive coupling of atomic systems to mesoscopic conductors. *Physical Review Letters*, 92(6):063601, Feb 2004.

[23] J. M. Raimond, M. Brune, and S. Haroche. Manipulating quantum entanglement with atoms and photons in a cavity. *Reviews of Modern Physics*, 73(3):565–582, Aug 2001.

[24] Pfeiffer Vacuum. *Vacuum Technology Know How*, pi0249pe edition, Feb 2010.

[25] Ray Radebaugh. Development of the pulse tube refrigerator as an efficient and reliable cryocooler. *Proceedings of the Institute of Refrigeration (London)*, 96, 1999/2000.

[26] S. Willitsch, J. Dyke, and F. Merkt. Generation and high-resolution photoelectron spectroscopy of small organic radicals in cold supersonic expansions. *Helvetica Chimica Acta*, 86:1152–1166, 2003.

[27] J. P. Marangos, N. Shen, H. Ma, M. H. R. Hutchinson, and J. P. Connerade. Broadly tunable vacuum-ultraviolet radiation source employing resonant enhanced sum-difference frequency mixing in krypton. *Journal of the Optical Society of America B: Optical Physics*, 7:1254–1263, 1990.

[28] Joseph L. Wiza. Microchannel plate detectors. *Nuclear Instruments and Methods*, 162:587–601, 1979.

[29] S. M. Sze. *Physics of Semiconductor Devices*. Wiley, second edition, 1981.

[30] Yu. M. Shwarts, V.L. Borblik, N.R. Kulish, V.N. Sokolov, M.M. Shwarts, and E.F. Venger. Silicon diode temperature sensor without a kink of the response curve in cryogenic temperature region. *Sensors and Actuators, A: Physical*, 76:107–111, 1999.

[31] Lake Shore Cryotronics, Inc. *Appendix C: Sensor Packaging and Installation*.

[32] Guy K. White. *Experimental Techniques in Low-Temperature Physics*. Clarendon Press, third edition, 1979.

[33] Frank Pobell. *Matter and Methods at Low Temperatures*. Springer, 2007.

[34] Allan G. Piersol and Thomas L. Paez. *Harris' Shock and Vibration Handbook*. McGraw-Hill, sixth edition, 2010.

[35] Osama A. B. Hassan. *Building Acoustics and Vibration*. World Scientific, 2009.

[36] Henry W. Ott. *Electromagnetic Compatibility Engineering*. Wiley, 2009.

[37] Ralph Morrison. *Grounding and Shielding, Circuits and Interference*. Wiley-Interscience, fifth edition, 2007.

[38] Jennifer Eve Hoffman. *A Search for Alternative Electronic Order in the High Temperature Superconductor $Bi_2Sr_2CaCu_2O_{8+\delta}$ by Scanning Tunneling Microscopy*. PhD thesis, University of California, Berkeley, 2003.

[39] Emile Hoskinson. Geophone calibration. Unpublished, June 2003.

[40] Steve Goldman. *Vibration Spectrum Analysis*. Industrial Press Inc., 1999.

[41] Colin Mercer. Acceleration, velocity and displacement spectra - omega arithmetic. Technical report, Prosig USA Inc., http://signalprocessing.prosig.com/OmegaArithmetic.pdf, 2006.

List of Figures

List of Tables

Appendices

Lake Shore Temperature Controller 340 Cabling

All Cables Overview

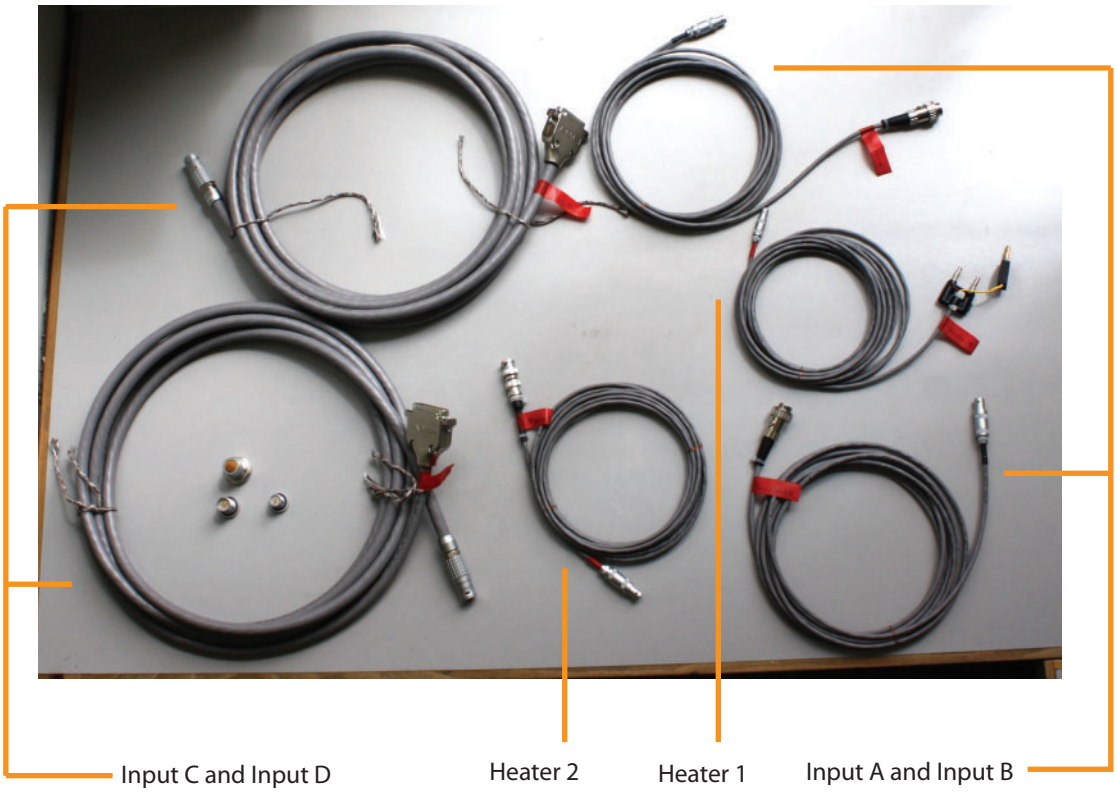

Cable lengths are approximately 4.70m. Twisted pairs are I+ with I- and V+ with V-. All shields are used.
Soldering tips:
- Tin wires before soldering.
- Use solder and flux separately, especially for solder cups and Lemo connectors.
- Use a shrinking hose for every wire if possible, otherwise use it in such a way that neighboring wires cannot be connected (use on every second wire).
- Make sure the connector strain relief works.
- Read the semester thesis of Christian Bolesch

Name	Jack(LSTC)	Plug(LSTC)	Cable	Plug(Cryo)	Jack(Cryo)
Heater 1	Banana Jacks 3 pins	Dual Banana & Laborstecker LS 410	Alpha Wire 5471C STP, 1x2 Wires	Lemo FFA.0S.302.CLAC42 2 pins	Lemo HGP.0S.302.CLLPV 2 pins, vacuum sealed
Heater 2	BNC Jack	BNC Jack & male-male BNC Adapter	Alpha Wire 5471C STP, 1x2 Wires	Lemo FFA.1S.304.CLAC42 4 pins	Lemo HGP.1S.304.CLLPV 4 pins, vacuum sealed
Input A & B	DIN 45322 6 pins	DIN 45322 6 pins	Alpha Wire 2466C STP, 2x2 Wires	Lemo FFA.1S.304.CLAC42 4 pins	Lemo HGP.1S.304.CLLPV 4 pins, vacuum sealed
Input C & D	D-Sub 25 pins	D-Sub 25 pins	Alpha Wire 6014C STP, 9x2 Wires	Lemo FGG.3B.324.CLAD12 24 pins	Lemo HGG.3B.324.CLLPV 24 pins, vacuum sealed

Heater 1 Cable

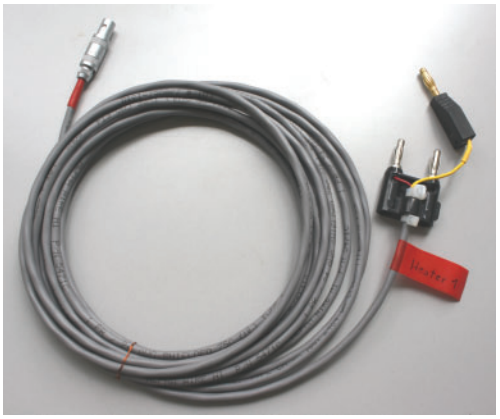

Jack (LSTC)

Dual Banana
Plug (LSTC)

Cable

Plug (Cryo)

Jack (Cryo), Rear View

Jack (Cryo), Front View

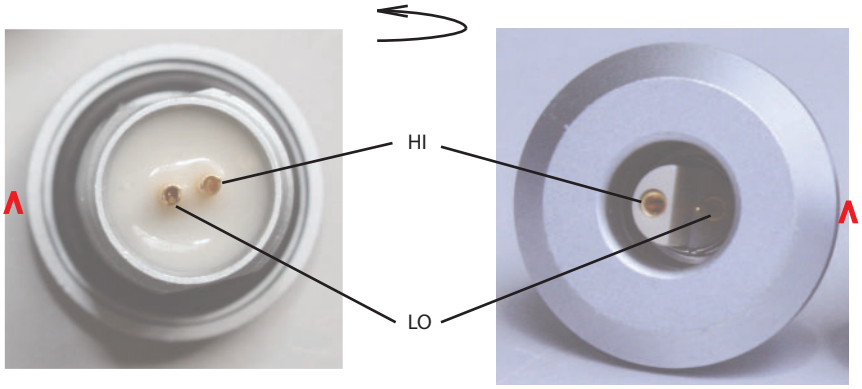

Heater 2 Cable

Jack (LSTC)

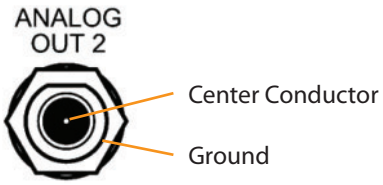

Plug (LSTC)

Cable
2 wires for Center Conductor & Ground, cable shield floating

Plug (Cryo)

Jack (Cryo), Rear View

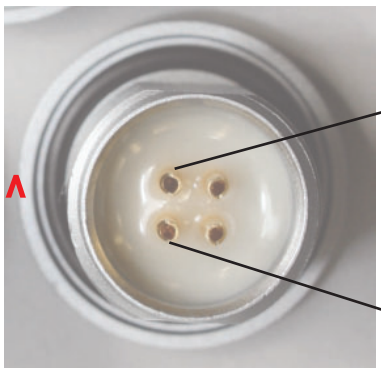

Jack (Cryo), Front View

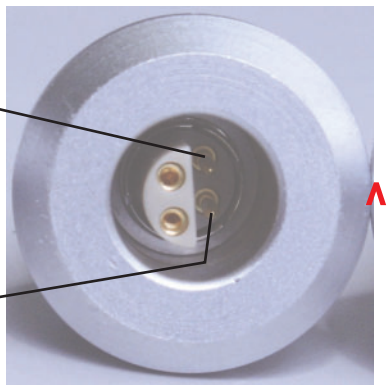

Center Conductor

Ground

Input A & B Cables

Jack (LSTC)

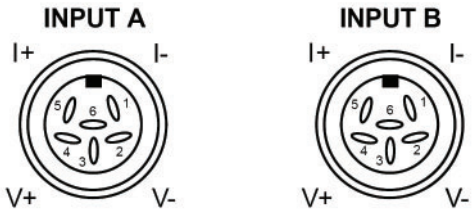

Plug (LSTC)

Cable

PIN	SYMBOL	DESCRIPTION
1	I–	– Current
2	V–	– Voltage
3	*none*	Driven Shield or Guard
4	+V	+ Voltage
5	+I	+ Current
6	*none*	No Connection

Plug (Cryo)

Jack (Cryo), Rear View

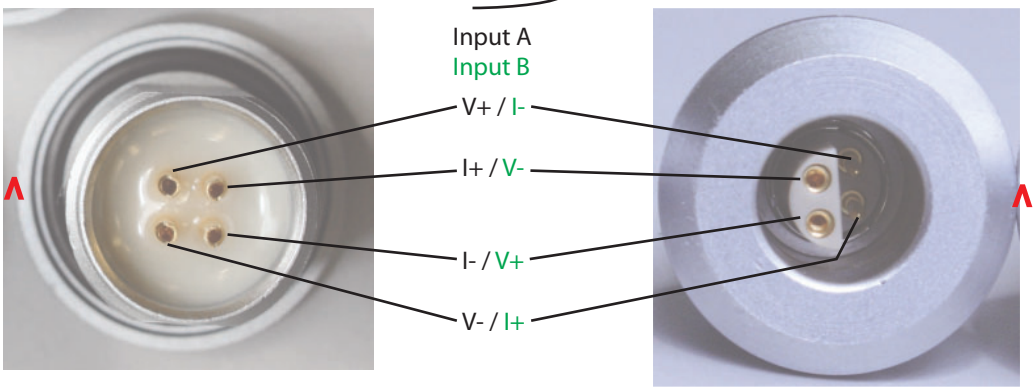

Input C & D Cables

Jack (LSTC)

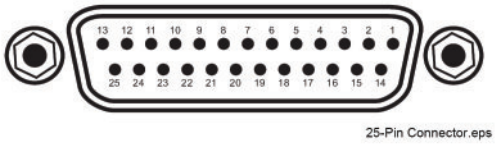

25-Pin Connector.eps

Plug (LSTC)

Cable

Input Connector (Input C)				Input Connector (Input D)			
PIN	DESC.	PIN	DESC.	PIN	DESC.	PIN	DESC.
1	NC			1	NC		
2	S	14	S	2	S	14	S
3	C1I+	15	C1I–	3	D1I+	15	D1I–
4	C1V+	16	C1V–	4	D1V+	16	D1V–
5	S	17	S	5	S	17	S
6	C2I+	18	C2I–	6	D2I+	18	D2I–
7	C2V+	19	C2V–	7	D2V+	19	D2V–
8	S	20	S	8	S	20	S
9	C3I+	21	C3I–	9	D3I+	21	D3I–
10	C3V+	22	C3V–	10	D3V+	22	D3V–
11	S	23	S	11	S	23	S
12	C4I+	24	C4I–	12	D4I+	24	D4I–
13	C4V+	25	C4V–	13	D4V+	25	D4V–

Plug (Cryo)

Jack (Cryo), Rear View, Zoomed

Jack (Cryo), Rear View

Jack (Cryo), Front View